Inverting surface soil moisture information from satellite altimetry over arid and semi-arid regions

B. Uebbing[a], E. Forootan[a,b], A. Braakmann-Folgmann[a], J. Kusche[a]

[a] *Institute of Geodesy and Geoinformation, University of Bonn, Bonn, Germany*
[b] *School of Earth and Ocean Sciences, Cardiff University, Cardiff, UK*

Abstract

Monitoring surface soil moisture (SSM) variability is essential for understanding hydrological processes, vegetation growth, and interactions between land and atmosphere. Due to sparse distribution of in-situ soil moisture networks, over the last two decades, several active and passive radar satellite missions have been launched to provide information that can be used to estimate surface conditions and subsequently soil moisture content of the upper few cm soil layers. Some recent studies reported the potential of satellite altimeter backscatter to estimate SSM, especially in arid and semi-arid regions. They also pointed out some difficulties of such technique including: (i) the noisy behavior of the backscatter estimations mainly caused by surface water in the radar foot-print, (ii) the assumptions for converting altimetry backscatter to SSM, and (iii) the need for interpolating between the tracks.

In this study, we introduce a new inversion framework to retrieve soil moisture information from along-track altimetry measurements. First, 20 Hz along-track nadir radar backscatter is estimated by post-processing waveforms from Jason-2 (Ku- and C-Band during 2008-2014) and Envisat (Ku- and S-Band during 2002-2008). This provides backscatter measurements every ∼300 m along-track within every ∼10 days from Jason, and every ∼35 days from Envisat observations. Empirical orthogonal base-functions (EOFs) are then derived from soil moisture simulations of a hydrological model, and used as constraints within the inversion. Finally, along-track altimetry reconstructed surface soil moisture (ARSSM) storage is inverted by fitting these EOFs to the altimeter backscatter. The framework is tested in arid and semi-arid Western Australia, for which a high resolution hydrological model (the Australian Water Resource Assessment, AWRA

Email addresses: uebbing@geod.uni-bonn.de (B. Uebbing), forootan@geod.uni-bonn.de (E. Forootan), s7anbraa@uni-bonn.de (A. Braakmann-Folgmann), kusche@geod.uni-bonn.de (J. Kusche)

model) is available. Our ARSSM products are also validated against Soil Moisture and Ocean Salinity (SMOS) L3 products, for which maximum correlation coefficients of bigger than 0.8 are found. Our results also indicate that ARSSM can validate the simulation of hydrological models at least at seasonal time scales.

Keywords: Altimetry, Backscatter, Altimetry Reconstructed Soil Moisture, Australia, Inversion

---

1. Introduction

Soil moisture storage is the main driver of the outgoing hydrological fluxes, such as evapotranspiration and (sub-)surface runoff (Katul et al., 2012), two important components of the terrestrial water cycle. Therefore, quantifying spatio-temporal variability of soil moisture is essential for modeling and understanding the water cycle, including land-atmosphere interactions, as well as for simulating present day and future climate change, and for flood and drought prediction (see, e.g., Rötzer et al., 2014). Nowadays, soil moisture remote sensing has attracted growing interest to complement the sparse available in-situ networks. The contribution of remote sensing techniques is in particular in monitoring of the top soil layer (first few centimeters).

Starting with the C-Band (5 GHz) wind-scatterometers on-board of the European Remote Sensing satellites ERS-1 (launched 1991) and ERS-2 (launched 1995), it was demonstrated that the scatterometer data could be applied to estimate vegetation and soil characteristics over continental land surfaces (Mougin et al., 1995). In fact, the backscattered signal energy is linked to the soil water content via the dielectric constant (Ulaby et al., 1982). In 2002, the National Aeronautics and Space Administration (NASA) launched the Aqua satellite mission that carried the Advanced Microwave Scanning Radiometer (AMSR-E) to observe (passive-mode) brightness temperatures at six dual polarized frequencies (Njoku et al., 2003). Lower microwave frequencies (e.g. C- or X-Band) allow a better monitoring of the upper few centimeters of the Earth's surface (Njoku et al., 2003) with reduced sensitivity to vegetation cover and surface roughness (Draper et al., 2009). To continue the coverage provided by the ERS missions, the Advanced Scatterometer (ASCAT) was launched in 2006 on-board a Meteorological Operational (METOP) satellite (Bartalis et al., 2007).

The Soil Moisture and Ocean Salinity (SMOS) satellite, a dedicated soil moisture monitoring mission, was launched in 2009 to provide brightness temperature and soil moisture products on a three-daily basis (Delwart et al., 2008; Montzka et al., 2013). Additionally, the Soil Moisture Active Passive (SMAP) mission (Entekhabi et al., 2010), launched in early 2015, has been monitoring continental soil moisture changes with its passive radiometer and active L-Band scatterometer. However, the active instrument failed after six month of operation. Table 1 provides a short summary on the individual missions.

Table 1: Summary of key features of individual soil moisture missions, as well as altimetry mission utilized in this study. Note that the across-track (act) resolution refers to the maximum distance between the tracks at the equator while the along-track (alt) refers to the distance between individual 20 Hz measurements. For SMAP we only report the spatial resolution of the passive radiometer.

Mission	**Launch**	**Sensor**	**Temporal Resolution**	**Spatial Resolution**
ERS-1/-2	1991/07	Scatterometer C-Band	3-4 d	50-60 km
Aqua	2002/05	AMSR-E: C-Band	3 d	75x43 km
METOP	2006/10	ASCAT: C-Band	2 d	50 km
SMOS	2009/11	MIRAS: L-Band	3 d	35 km
SMAP	2015/01	L-Band	2-3 d	40 km
Envisat	2002/03	active Ku- and S-Band	35 d	300 m alt, 80 km act
Jason-2	2008/07	active Ku- and C-Band	10 d	300 m alt, 315 km act

Dedicated satellite altimetry missions (e.g., Envisat, Topex/Poseidon and its follow-on Jason 1, 2, and 3) have been originally designed to measure sea surface height over the oceans (Shum et al., 1995). Over land, the measured backscatter is closely related to soil characteristics at the satellite nadir (Papa et al., 2003; Blarel et al., 2015). Ridley et al. (1996) and Fatras et al. (2012) found high correlation between in-situ soil moisture measurements and altimetry backscatter from the Topex/Poseidon and Envisat missions. Fatras et al. (2015) extended these investigations to different land cover regions, such as desert, savanna and forests. They compared Jason-2 backscatter with side-looking scatterometers (QuickSCAT and ASCAT) over the arid regions of West Africa and found altimetry results to be more sensitive to soil moisture variations and considerably less to vegetation effects, due to the nadir-looking instrument on-board of the satellite. Ka-Band measurements of the Satellite with Argos and Altika (SARAL) mission were assessed by Frappart et al. (2015) to relate the backscatter estimates to spatio-temporal changes in surface roughness, land cover, and soil moisture changes over West Africa. Their study indicates that Ka-Band measurements are able to penetrate underneath the canopy of tropical forests in non-inundated areas. In Table 2, relevant studies that utilize altimetry for soil moisture studies are summarized. We believe that altimetry missions (1) provide high resolution along-track measurements ($\sim$300 m) of backscatter with (2) low sensitivity to vegetation in combination with (3) more than two decades of continuous measurements which makes altimetry a valuable and independent tool for measuring surface soil moisture. However, due to the limited (across-track) spatial and temporal resolution (Table 1), the range of applications for altimetry based soil moisture monitoring might be limited and the data should be utilized in combination with the existing dedicated soil moisture missions.

Estimating surface soil moisture (SSM) from brightness temperatures as measured by dedicated soil moisture missions, or from backscatter observations as measured by altimetry, is challenging. Several previous studies formulated this conversion based on a linear change detection approach (Wagner et al., 1999) and applied to SMOS observations. For example, Liu et al. (2011) combined active (ASCAT) and passive (AMSR-E) products and rescaled them against the simulation of the Global Land Data Assimilation System (GLDAS, Rodell et al., 2004). In Piles et al. (2011), SMOS products were combined and downscaled to 1 km using high resolution VIS/IR MODIS observations. Al-Yaari et al. (2015) applied a multiple-linear regression approach to minimize the differences between AMSR-E and SMOS soil moisture products. An artificial neural network was used to estimate soil moisture from simulated brightness temperatures as in Liou et al. (2001), Angiuli et al. (2008), and Chai et al. (2010). Recently, Rodríguez-Fernández et al. (2015) applied a neural network to identify the statistical relationship between a reference soil moisture data set and a variety of information from SMOS brightness temperatures, C-Band backscatter coefficients from ASCAT and MODIS derived Normalized Difference Vegetation Index (NDVI) data.

Converting altimetry backscatter to soil moisture storage is accompanied with difficulties including (i) the noisy behavior of the backscatter estimates as a result of strong reflections from surface water in the radar footprint or variations of surface roughness, (ii) the assumptions, such as homogeneous surface conditions in the radar footprint, and (iii) the need of interpolation between the altimetry tracks. In this study, we present a novel approach to retrieve soil moisture from satellite altimetry backscatter measurements. The main objectives are:

1. to develop an inversion approach which utilizes spatial patterns of modeled soil moisture to constrain altimetry backscatter and estimate meaningful surface soil moisture (SSM) information along the altimeter track (Section 4.2);
2. to validate the altimetry reconstructed SSM estimates by comparing them with model simulations and with satellite products (e.g. Section 5.2 and 5.3); and
3. to explore the behavior of altimetry derived SSM within regions with varying land cover, soil moisture content and topography (e.g. Section 6.3).

Table 2: Studies that utilize satellite altimetry backscatter in context of examining SSM.

Study	Data used	Location	Key results
Ridley et al. (1996)	Topex Ku- and C-Band, modeled backscatter from surface roughness, soil moisture, vegetation, and topography	Simpson Desert, Australia	**1.** Soil moisture is found to be the dominant component **2.** No significant temporal variation is found due to changes in topography and vegetation cover **3.** Effects from precipitation on soil moisture decay after about 2 days
Papa et al. (2003)	Topex Ku- and C-Band and C-minus Ku-Band	global	**1.** Backscatter is related to soil characteristics **2.** Altimetry has the potential to monitor land surfaces at global and regional scales
Fatras et al. (2012)	Envisat Ku- and S-Band, in-situ soil moisture station, ASCAT data	Sahel region, Mali	**1.** Linear relationship is considered between backscatter and SSM **2.** Vegetation influence on SSM from altimetry is small **3.** Quality of SSM from altimetry using a change detection approach depends on distance to the in-situ station, presence of open water surfaces, topography, and chosen retracking algorithm.
Fatras et al. (2015)	Jason-2 Ku- and C-Band, Envisat Ku-Band, QuikSCAT and ASCAT scatterometry data	West Africa	**1.** Nadir-looking altimeters are found to be more sensitive to SSM than side-looking scatterometers **2.** Impact of vegetation on altimetry backscatter is low **3.** Magnitudes of band-dependent backscatter change over different surface types
Frappart et al. (2015)	Jason-2 Ku- and C-Band, Envisat Ku- and S-Band, Saral/Altika Ka-Band	West Africa	**1.** Altimeter radar echos at nadir incidence are well correlated to soil moisture in semi-arid areas **2.** Altimeters are able to detect the presence of water even under dense canopies at all frequencies **3.** Only Ka-Band is found capable of penetrating underneath the canopy of non-inundated tropical forest

This study	Jason-2 Ku- and C-Band, Envisat Ku-Band, SMOS derived SSM, AWRA and GLDAS top level soil moisture model data, and ERA-Interim precipitation	Western Australia, Australia	**1.** Spatial patterns extracted from model data are used to constrain measured backscatter and to convert to SSM **2.** Inversion approach **3.** Validation against model data and SMOS derived SSM indicates good agreements within (semi-)arid regions with varying land cover, surface roughness, vegetation coverage and human influence

2. Study Area

We select a large part of the semi-arid and arid Western Australia as our study area, which covers about one third of the continent i.e. an area of approximately 2.53 million square kilometers. In contrast to earlier studies (Piles et al., 2011; van der Schalie et al., 2015), no in-situ networks of terrestrial soil moisture stations are available here. In the northwest and central parts, the predominant climate is semi-arid to arid, and in the southwest, a more temperate semi-arid to Mediterranean climate can be found. Top level soil moisture in Western Australia is primarily driven by precipitation suggesting a strong land-atmosphere coupling (Bartalis et al., 2007; Draper et al., 2009). This will provide an opportunity to compare estimated altimetry derived soil moisture patterns with those from a global and a continental land surface model. The central part of Western Australia is relatively dry with sparse vegetation coverage (Donohue et al., 2008; Glenn et al., 2011, Fig. 1 and 2), thus, it makes a good study area to test the proposed framework, although, we do not expect a significant contribution of vegetation cover in the altimetry backscatter (Frappart et al., 2015). Two sub-regions are considered in this study. Region A (area of about 1.47 million square kilometers), is defined by longitudes from $113°E$ to $126°E$ and latitudes between $30°S$ and $18°S$ in Fig. 1 (left), including the (semi-)arid northern and central part of Western Australia. Region B (area of about 0.37 million square kilometers) is defined within the longitude bounds $114°E$ to $122°E$ and latitude bounds $35°S$ to $30°S$ in Fig. 1 (right), and covers the southwest of the continent. General land cover classes within both regions derived from MODIS are shown in Fig. 1. Classification is implemented according to the International Geosphere Biosphere Programme (IGBP) scheme by the 'AusCover' facility available from the Terrestrial Ecosystem Research Network (TERN, `http://www.auscover.org.au/`).

In region A, the surface is mostly covered by shrublands mixed with grassland and savanna, especially in the western central part, while in the north and northeast of region A, the coverage is denser. In region B, pronounced variation in land cover can be found, ranging from dryer shrubland and savanna regions in the northeast and east to the wetter southwest area. Agricultural land use can be seen in the central and western parts, as well as some forest areas in the southwest.

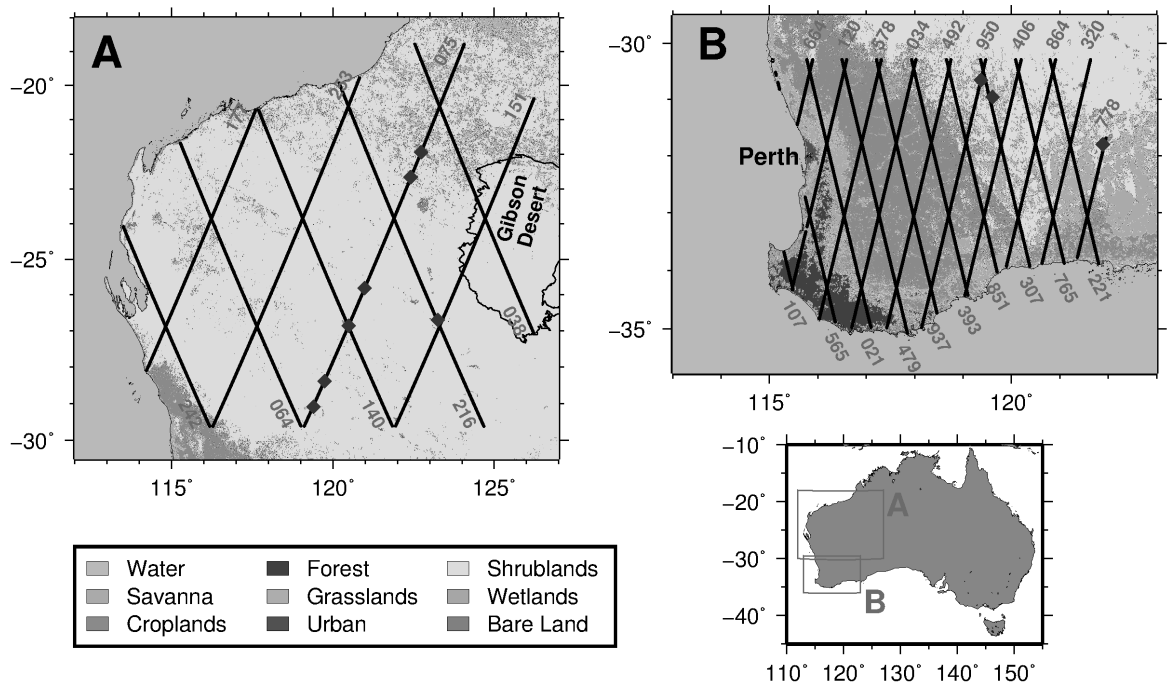

Figure 1: Study areas A and B, where soil moisture information is extracted from satellite altimetry within Western Australia. Land cover classes for the year 2008 are shown. (A) The case study in the northern part of Western Australia used for estimating ARSSM from Jason-2 observations, and (B) includes the southern part of Western Australia utilized for estimating ARSN from Envisat observations. The black lines denote the Jason-2 and Envisat nominal repeat tracks. The corresponding pass numbers are shown close to the tracks. The blue diamonds indicate the locations of surface waters along track 075 (Sec. 4.1, Fig. 2) and the lakes which are explicitly mentioned in the following text.

3. Data

3.1. Satellite Radar Altimetry Observations

Observed waveforms from the Sensor Geophysical Data Records (SGDR) of the Jason-2 (2008-2014) and European Environmental Satellite (Envisat, 2002-2010) missions are used to derive backscatter (σ_0) information. For both missions the diameter of the pulse limited footprint is between 2-10 km depending on topography over land surfaces (Chelton et al., 2001).

Jason-2: The Ocean Surface Topography Mission (OSTM) / Jason-2 mission was launched in June, 2008 as a follow-on mission to Jason-1. The satellite orbits the Earth in a near circular ~10-day repeat orbit at an altitude of approximately 1336 km with an inclination of 66 deg and a groundtrack separation of about 315 km at the equator. The instruments on board of the satellite include the altimeter, a radiometer for deriving wet troposphere corrections, as well as GPS and DORIS systems for precise orbit determination (Desjonquères et al., 2010). The Poseidon-3 altimeter on board Jason-2 emits radar pulses at Ku-Band (13.575 GHz/2.21 cm) and C-Band (5.3 GHz/5.08 cm) to derive ionospheric electron content influencing the radar signal (Desjonquères et al., 2010; AVISO, 2015). Jason-2 SGDR data include the 20 Hz positions, Ku- and C-Band waveforms, corresponding scaling factors, and automatic gain control (AGC) information, as well as 1 Hz atmospheric backscatter attenuation corrections and quality flags. However, the flags may not be fully reliable over land influenced regions (Birkett & Beckley, 2010). The Jason-2 data have been acquired from the CNES Archiving, Validation and Interpretation of Satellite Oceanographic (AVISO) team (`ftp://avisoftp.cnes.fr/AVISO/pub/jason-2/`). Backscatter information within region A is estimated by reprocessing Jason-2 waveforms between mid of 2008 and end of 2014 according to section 4.1. The nine Jason-2 tracks with their identification numbers are displayed in Fig. 1 (A).

Envisat: The Envisat satellite was launched in March, 2002 as a follow-on mission to ESA's ERS-1 and ERS-2 missions. The satellite flies on a ~35-day sun-synchronous repeat orbit with an altitude of 800 km and inclination of 98.55 deg. This results in a groundtrack separation of approximately 80 km at the equator. Among the 10 instruments on the satellite, a microwave radiometer that allows estimating the liquid water content of the atmosphere, and the DORIS positioning system and retro reflectors for ground bases satellite laser ranging (SLR) enable precise orbit determination (Zelli, 1999). The Radar Altimeter 2 (RA2) altimetry instrument operates in Ku-Band (13.575 GHz/2.2 cm) and S-Band (3.2 GHz/9.37 cm) (ESA, 2007). However, on January

18, 2008 the S-Band transmission power dropped significantly, rendering all S-Band observation from this date onward unfeasible. Envisat observations (2002-2010) are examined over the region B in Fig. 1 (B). The distances between Envisat repeat tracks are smaller then those of Jason-2. The Envisat RA2 data was provided to this study by the European Space Agency (ESA, `https://earth.esa.int/`).

3.2. Land Surface Model Data

A-priori soil moisture data is required to derive EOFs within the proposed inversion (see section 4.2). In this study, we use top layer soil moisture from the Global Land Data Assimilation System (GLDAS) (Rodell et al., 2004) and from the Australian Water Resources Assessment (AWRA) system (Vaze et al., 2013).

GLDAS: We use 3-hourly GLDAS-2.1 land surface model data produced by NOAH and available through the Goddard Earth Sciences Data and Information Services Center (`http://disc.sci.gsfc.nasa.gov/services/grads-gds/gldas`) with a resolution of 1 degree. The soil moisture is provided in 4 layers (0-10 cm, 10-40 cm, 40-100 cm and 100-200 cm) in units of kg/m^2. In this study, we utilize the water storage of the first layer since the altimeter backscatter derived from Ku- and C-Band (or S-Band) frequencies is only sensitive to the first few centimeters of the soil water content.

AWRA: The AWRA Landscape model (AWRA-L) simulates evapotranspiration, runoff, and soil moisture for the Australian continent on a 0.05 deg ($\sim$5.5 km) grid. AWRA employs two hydrological response units (HRU) corresponding to different vegetation root depths. Before combining the two flux and storage outputs, the HRUs are modeled separately, e.g., considering varying access to individual soil layers. The soil moisture information is subdivided into upper (0-10 cm), lower (10-100 cm) and deep (100-600 cm) layers. For this study, we used daily top-layer soil moisture provided by the Commonwealth Scientific and Industrial Research Organization (CISRO). The soil moisture values are scaled between 0 and 1 in units of m^3/m^3, with a maximum capacity value for top-layer water storage of 3 cm, which means that the model values are capped at $0.3\,m^3/m^3$.

3.3. ERA-Interim Precipitation Reanalysis

ERA-Interim precipitation reanalysis data (Dee et al., 2011) is available from the European Centre for Medium-Range Weather Forecasts (ECMWF). The data product is available from `http://www.ecmwf.int/`. In this study, we utilize global grids with 0.75° resolution of total precipitation in meters from 2002 to 2014 which are available every twelve hours at 12 p.m. and 12 a.m., respectively. The data have been accumulated for the last 3-days before the altimeter crossing the study area in order to validate the altimeters' ability to detect past rainfall events of several days before (Ridley et al., 1996).

3.4. Soil Moisture and Ocean Salinity (SMOS) Products

Daily level-3 products from the ESA-satellite SMOS are available from `http://cp34-bec.cmima.csic.es/land-datasets/`, based on the level-2 soil moisture User Data Product (UDP) (SMOS-BEC, 2015). The SMOS satellite covers the total surface of the Earth every three days. The daily grids with a resolution over Australia of about 0.25° include only the last overflight within each three days and the data product is divided into ascending and descending tracks, with the ascending data referring to approximately 6 a.m. and the descending data referring to approximately 6 p.m. local time. The soil moisture information is provided in terms of percentage, between 0 and 1 (ESA, 2014). Soil moisture values derived from SMOS L3 ('SMOS' from now on) over Western Australia are found mostly in the range of 0 to 0.5, where 0.5 corresponds to $0.5m^3$ of water per $1m^3$ of soil.

4. Methods

Backscatter nadir measurements at a rate of 20 Hz (every ∼300 m along-track) of Jason-2 (Ku- and C-Band) and Envisat (Ku- and S-Band) altimetry missions, that provide new measurements every ∼10 days (Jason-2, 2008 - 2014) or ∼35 days (Envisat, 2002 - 2010), are examined over the arid and semi-arid Western Australia.

The proposed inversion approach consists of four steps: (i) along-track backscatter are estimated by post-processing the altimetry waveforms as described in section 4.1. (ii)

Principal Component Analysis (PCA, Preisendorfer, 1988) is applied to extract the dominant orthogonal modes of top level soil moisture storage simulated by either a global or regional hydrological model along the altimetry tracks in (i). (iii) We employ all available spatial empirical orthogonal functions (EOFs) of (ii), and use them in an inversion procedure as a-priori information (base-functions) for fitting to the backscatter observations of (i). (iv) The results of step (iii) are the altimetry derived temporal variability that are used to derive altimeter reconstructed surface soil moisture (ARSSM) products that represent the top soil level storage changes (see section 4.2 for details).

Our results suggest that the proposed method works well in different regions. Here, we validate the results in a (semi-)arid region because this allows us to neglect influences on the backscatter measurement, e.g. seasonal variations in snow cover, which otherwise would have to be removed from observations. For validation, we compare our reconstructed SSM to reanalysis precipitation data from ERA-Interim (Dee et al., 2011). Our assumption is that rainfall is the main driver of soil moisture in the semi-arid regions, as well as to top level soil moisture extracted from global and regional models. Furthermore, we assess the differences with respect to SMOS L3 soil moisture (SMOS-BEC, 2015).

4.1. Processing Altimeter Waveforms

Backscatter (σ_0) can be estimated by post-processing altimetry waveforms as (ESA, 2007)

$$\sigma_0 = s + q + \Delta_{atm}, \tag{1}$$

with

$$q = 10 \log_{10}(Pu), \tag{2}$$

where q is the term derived from retracking the altimeter return waveform and converting the estimated amplitude Pu to decibel using equation (2). In equation (1), Δ_{atm} is the atmospheric attenuation of the backscatter, provided in the SGDR data, and s is the scaling factor that is derived from the radar equation applied to satellite altimetry (Roca et al., 2002). The scaling factor is computed by the Envisat and Jason-2 processing centers and provided in the SGDR data.

The shape of the altimeter return waveform over land surfaces usually does not correspond well to known model shapes from open water surfaces, such as the Brown model (Brown, 1977). Off-nadir surface waters, such as lakes or rivers, introduce peaks into the waveform, which will significantly influence the geophysical parameters, especially the amplitude Pu that is computed following Deng et al. (2002)

$$Pu = \sqrt{\frac{\sum_{i=1}^{N} P_i^4(t)}{\sum_{i=1}^{N} P_i^2(t)}}, \tag{3}$$

with the number of range gates N, and P_i being the return power at the i'th range gate. Combining equations (1), (2) and (3) will result in backscatter estimates very similar to the Off Center Of Gravity (OCOG) or threshold methods, such as ICE-1 which is included in the GDR data. To suppress the energy from individual off-nadir peaks, related to surface waters inside the altimeter footprint, we convert the total waveform to decibel using equation (4)

$$\tilde{P_i} = 10\log_{10}(P_i). \tag{4}$$

We replace P_i in equation (3) with estimated $\tilde{P_i}$ from equation (4) to compute modified amplitudes $\tilde{Pu}$ whose unit is decibel and can replace q in equation (1) to estimate modified backscatter. The original backscatter (from equations (1), (2), and (3)) shows relatively larger along-track variations compared to our modified approach, which is considerably less affected by small peaks on the waveform's trailing edge which we ascribe to small off-nadir surface waters. In Fig. 2, we correlate the original and modified along-track backscatter values from Jason-2 with the top level soil moisture information from the AWRA model. The results indicate higher correlation between the smoother backscatter estimations $\tilde{\sigma}_0$ from the modified approach with AWRA compared to the backscatter results (σ_0) from the original approach. Large peaks appear in Fig. 2 (gray regions), which are related to the strong reflection from surface water. These include Lakes Barlee, Noondie, Way, Teague, and Dora, as well as the Rundall River, which are also marked in Fig. 1.

The magnitude of the backscatter value is mainly defined by the scaling factor and the corresponding automatic gain control (AGC) value, while the 2nd term in equation (1) only slightly changes the final results. As a result, the backscatter value (σ^0 derived from equation (1)) still peaks when the altimeter nadir is close to surface waters. In order to reduce the influence from surface waters, we compute the difference of along-track backscatter measurements from consecutive altimetry cycles. This reduces the influence of slowly varying surface features such as surface roughness, and to some extent, dynamic changes, e.g., vegetation growth. Therefore, backscatter anomalies (instead of absolute backscatter) are used to compute soil moisture anomalies.

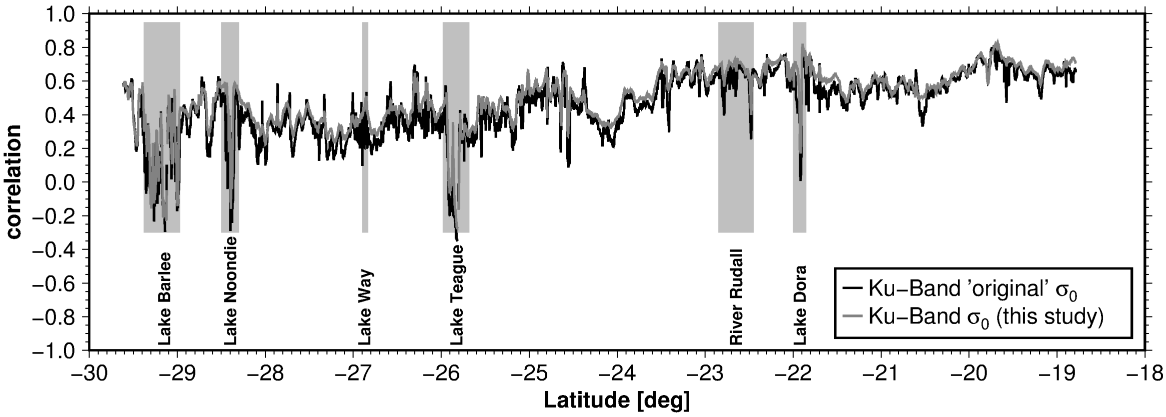

Figure 2: Correlation coefficients between Ku-Band backscatter (σ_0) with AWRA model data along the pass 075 of Jason-2. Two correlation coefficient curves are shown, for σ_0 processed by the original method (black curve, derived from equations (1), (2) and (3)), and the orange curve represents the modified approach. We found similar correlation results from the C-Band backscatter estimations.

4.2. An Inversion Framework for Converting Backscatter to Soil Moisture Storage

Spatio-temporal variability of altimetry backscatter (denoted by the subscript B) and of soil moisture storage (denoted by the subscript S) can be arranged in a data matrix $\mathbf{X}_{\mathrm{B/S}}(t, j)$, with t representing the time of observations and j standing for their positions. We assume that the time series are already centered, i.e. their temporal mean has already been reduced. The data matrix can be decomposed by Singular Value Decomposition (SVD, Preisendorfer, 1988) as

$$\mathbf{X}_{\mathrm{B/S}}(t, j) = \bar{\mathbf{P}}_{\mathrm{B/S}}(t)\ \mathbf{\Lambda}_{\mathrm{B/S}}\ \bar{\mathbf{E}}^{T}_{\mathrm{B/S}}(j), \tag{5}$$

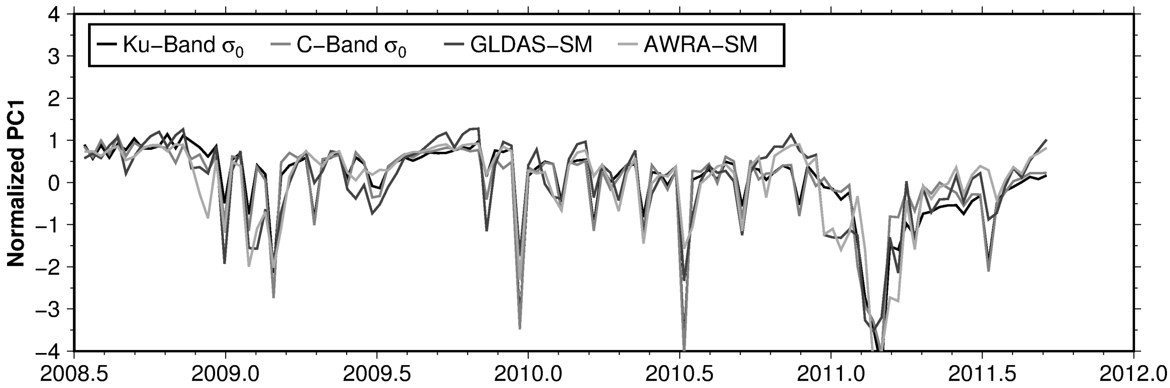

Figure 3: Normalized first principal component (PC) derived by applying equation (5) to along-track altimetry backscatter (σ_0 data from Ku- (35.1%) and C-Band (40.3%)), as well as top level soil moisture simulations of GLDAS (65.6%) and AWRA (44.5%). The PCs are computed along the track 075 of Jason-2 in the northern study area (Fig. 1, region A). All principal components are normalized by their standard deviation. The percentage values in parenthesis provide the amount of total variance explained by the corresponding first PCs.

where $\bar{\mathbf{P}}_{\mathrm{B/S}}(t)$ contains normalized temporal principal components (PCs), $\mathbf{\Lambda}_{\mathrm{B/S}}$ is a diagonal matrix that holds the singular values λ ordered according to their magnitude, and $\bar{\mathbf{E}}_{\mathrm{B/S}}(j)$ contains the spatial empirical orthogonal functions (EOFs). PCA allows to extract a large amount of variance (of $\mathbf{X}_{\mathrm{B/S}}$) in relatively few orthogonal modes. PCs ($\bar{\mathbf{P}}_{\mathrm{B/S}}(t)$) and EOFs ($\bar{\mathbf{E}}_{\mathrm{B/S}}(j)$) in equation (5) are unit-less and orthogonal, i.e. $\bar{\mathbf{P}}^T_{\mathrm{B/S}}(t)\bar{\mathbf{P}}_{\mathrm{B/S}}(t) = \mathbf{I}$ and $\bar{\mathbf{E}}^T_{\mathrm{B/S}}(j)\bar{\mathbf{E}}_{\mathrm{B/S}}(j) = \mathbf{I}$ with $\mathbf{I}$ being the identity matrix. We use them as base-functions for comparing altimetry backscatter estimations and model derived soil moisture storage or combining them. The standard deviation of variability in the data matrix $\mathbf{X}_{\mathrm{B/S}}$ and the measurement unit is reflected in $\mathbf{\Lambda}_{\mathrm{B/S}}$, which can be used to relate anomalies of altimetry backscatter to SSM changes.

To investigate whether there is a connection between backscatter and soil moisture, we apply equation (5) to the altimetry derived backscatter $\tilde{\sigma}_0$ from along-track Jason-2, Ku- and C-Band (Fig. 3), as well as the top level soil moisture from the GLDAS and AWRA models along the same track. Here, only the temporal evolution of the first dominant PC is shown, for which we find a correlation coefficient of about 0.8 between altimetry backscatter and AWRA/GLDAS derived soil moisture simulations. This provides us with confidence that altimetry backscatter mainly reflect soil moisture variations. The resulting EOFs from GLDAS and AWRA generally agree with the EOFs from GLDAS but show a smoother profile along the track due to the lower spatial resolution of the GLDAS model data.

Considering equation (5), if the altimetry backscatter estimations were linearly related to the soil storage changes, one could conclude that $\bar{\mathbf{P}}_{\mathrm{B}}$ and $\bar{\mathbf{E}}_{\mathrm{B}}$ are also linearly related to $\bar{\mathbf{P}}_{\mathrm{S}}$ and $\bar{\mathbf{E}}_{\mathrm{S}}$, respectively. This is however not true considering the relationship in equations (1) to (4), and due to the differences between noise distribution of backscatter and soil moisture storage simulations. Therefore, we propose an inversion method to convert backscatter to soil moisture storage estimations. This can be realized by fitting the EOFs of the model derived soil storage ($\bar{\mathbf{E}}_{\mathrm{S}}$) to the altimetry backscatter estimations ($\mathbf{X}_{\mathrm{B}}$) as

$$\hat{\bar{\mathbf{P}}}(t) = \mathbf{\Lambda}_{\mathrm{B}}^{-1} \, [\bar{\mathbf{E}}_{\mathrm{S}}^{T}(j) \; \bar{\mathbf{E}}_{\mathrm{S}}(j)]^{-1} \; \bar{\mathbf{E}}_{\mathrm{S}}^{T}(j) \; \mathbf{X}_{\mathrm{B}}(t, j). \tag{6}$$

In this estimation, we rely on the spatial distribution of soil moisture storage from a model. Therefore, $\bar{\mathbf{E}}_{\mathrm{S}}$ are chosen as base-functions that remain invariant within the inversion. The term $\mathbf{\Lambda}_{\mathrm{B}}^{-1}$ makes the backscatter estimations unit-less. After solving equation (6), updated temporal patterns ($\hat{\bar{\mathbf{P}}}$) are estimated that indicate the contribution of soil moisture storage changes in the backscatter estimations. Finally, altimetry backscatter are converted to soil moisture storage variability by a PCA reconstruction as

$$\hat{\mathbf{X}}_{\mathrm{S}}(t, j) = \hat{\bar{\mathbf{P}}}(t) \; \mathbf{\Lambda}_{\mathrm{S}} \; \bar{\mathbf{E}}_{\mathrm{S}}^{T}(j). \tag{7}$$

$$\hat{\mathbf{X}}_{sm}(t, s) = \hat{\bar{\mathbf{P}}}(t) \; \mathbf{\Lambda}_{\mathrm{sm}} \; \bar{\mathbf{E}}_{\mathrm{sm}}^{T}(s) \tag{8}$$

$$\hat{\bar{\mathbf{P}}}(t) = \mathbf{\Lambda}_{\sigma_0}^{-1} \, [\bar{\mathbf{E}}_{\mathrm{sm}}^{T}(s) \; \bar{\mathbf{E}}_{\mathrm{sm}}(s)]^{-1} \; \bar{\mathbf{E}}_{\mathrm{sm}}^{T}(s) \; \sigma_0(t, s) \tag{9}$$

$$\mathbf{X}(t, s) = \bar{\mathbf{P}}(t) \; \mathbf{\Lambda} \; \bar{\mathbf{E}}^{T}(s) \tag{10}$$

5. Results

In the following, the results of estimated altimetry reconstructed surface soil moisture (ARSSM, equation (7)) are presented and compared to model simulations and to independent SSM measurements from SMOS. The model simulations and gridded SMOS data are spatially interpolated to the position of the altimetry tracks. Temporally, we also interpolated the data according to the times when the altimeter crosses the study sites. We then compute differences between backscatter from successive altimetry cycles in order to reduce the signal from constant and slowly changing influences, such as surface roughness or vegetation. For consistency, the same differences are applied to the interpolated model and SMOS data, i.e. we estimate anomalies for each data set along the altimetry tracks. To implement the proposed inversion, we apply PCA to GLDAS and AWRA data, resulting in 34 and 117 EOFs, respectively. For both models, we keep the EOFs that correspond to at least 99% of the variance, i.e. 20 EOFs for GLDAS and 25 for AWRA.

First, the consistency of our ARSSM is examined by computing annual amplitudes and phases and comparing to amplitudes and phases derived from GLDAS and AWRA. Afterwards, along-track comparisons are presented before the investigation is extended to all Jason-2 groundtracks located inside the study region A, and all Envisat groundtracks within the study region B (Fig. 1). Finally, we will examine the differences between soil moisture model simulations and ARSSM estimates. To better visualize the surface topography impact on the estimated ARSSM (e.g., Fig. 4), we use elevation information derived from the SRTM30plus V11 data set (`http://topex.ucsd.edu/WWW_html/srtm30_plus.html`). Spatial anomalies of topography changes, derived from subtracting the topography smoothed by a 100km Gaussian filter, are also shown as gray shaded background that likely represent the geometrical roughness. In our study sites, land elevation and spatial anomaly rarely exceed 1000m and 100m, respectively.

5.1. Assessing the Level of Agreement between the ARSSM and Model Simulation/ SMOS

To assess the consistency of the ARSSM, we have computed the annual amplitudes and phases from our inversion results, as well as from the GLDAS and AWRA model data

(Fig. 4). Generally we find relatively small amplitudes in the range of ∼0 to 0.01 m^3/m^3 which vary along the individual tracks with higher amplitudes closer to the coast in the North, as well as over the agricultural areas in the South-West. For the phase component we find similar transition of about 300 days in the South-West to about 60 days in the North-East for ARSSM and the two model data sets. Over the Gibson Desert (Fig. 1, (A)), zero amplitudes from ARSSM (Fig. 4, (A)) and the AWRA model (Fig. 4, (E)) are detected, while significant signal is found from the GLDAS model (Fig. 4, (C)). In the central and southern central parts of our study region, the magnitude of the amplitudes from ARSSM (Fig. 4, (A)) tend to agree better with the ones from GLDAS (Fig. 4, (C)) compared to the amplitudes from AWRA (Fig. 4, (E)). We do not find any patterns coinciding with dominant topographic features shown in the background of the sub-figures. The GLDAS phases (Fig. 4, (D)) show less spatial variation compared to the AWRA and ARSSM phases.

In Fig. 5 (A) and (B), we directly compare ARSSM anomalies, derived using EOFs from AWRA, with surface soil moisture anomalies from AWRA (A) and SMOS (B) during one arbitrarily chosen date, January 31, 2010, when the Jason-2 satellite was crossing the study site A. The track is outlined by a black polygon and the colors inside represent the ARSSM anomalies. The spatial features of AWRA and SMOS generally agree as both, provide negative anomalies in the north and strong positive anomalies in the central parts. However, although we utilized EOFs from AWRA to derive the ARSSM, Fig. 5 (A) shows only weak agreement between AWRA model data and ARSSM on the chosen date. In contrast, ARSSM generally agrees well with the SMOS product in the southern and central parts of the track. In the north, we detect weaker anomalies compared to SMOS (Fig. 5, (B)).

5.2. Along-Track Behavior of the ARSSM

The results of this section refer to the pass 075 of Jason-2 (within region A of Fig. 1). Between the latitude of 30°S to 24°S, the land cover is mainly shrublands, while in the north (between 24°S and 18°S), it changes to a mix of shrublands, grasslands and savanna. Four sets of ARSSM products are estimated from either Ku- and C-Band while using the EOFs of GLDAS or AWRA in the inversion (equation (6)). A strong agreement is found between GLDAS and AWRA simulations along the pass 075 of Jason-2, whereas both products are highly correlated (correlation coefficients of 0.6 to 0.8) as shown in Fig. 6. For brevity, we show the ARSSM results based on AWRA EOFs in Fig. 6.

Correlation between ARSSM (from Ku- and C-Band) with AWRA is slightly lower than between GLDAS and AWRA, but the ARSSM results suggest a similar quality compared to the SMOS product in the southern part of the track, while ARSSM provides higher correlation coefficients than SMOS in the north. Unlike the correlation coefficients between altimetry backscatter and AWRA (Fig. 2), the ARSSM results do not exhibit large peaks close to the larger surface waters. Our results indicate that soil moisture retrieved from the ascending orbit of SMOS (dashed cyan line) is better correlated with AWRA simulations compared to those derived from the descending orbit (solid cyan line). Additionally, Fig. 6 shows the correlation with respect to the difference of ARSSM estimated from C- minus Ku-Band observations (blue line), which suggest considerably less similarity with model simulations. Therefore, they will no longer be discussed in this paper.

Considering the magnitude of correlation coefficients along the altimeter track in Fig. 6, in the south (up to a latitude of $\sim 24°S$), one can see smaller values (around 0.4) between ARSSM, as well as SMOS soil moisture and AWRA simulations. To the north, correlation coefficients between ARSSM and AWRA rise to around 0.6 with some points being bigger than 0.7, while those of SMOS do not increase significantly. This behavior coincides roughly with the change of land cover classes from shrublands only in the south to a mixture of shrublands, grasslands and savanna in the north part of Fig. 1 (A). Additionally, the topography in the north is less mountainous, which results in more reliable backscatter measurements and consequently ARSSM estimation.

To understand the short-term impact of precipitation on the surface soil moisture variability in this region, we compare model simulations, SMOS, and our ARSSM with 3-day accumulated precipitation anomalies derived from the ERA-Interim reanalysis product (Fig. 7). Generally, the correlation coefficients between ARSSM (from both Ku- and C-Band observations) and precipitation are larger compared to those between precipitation and the GLDAS or AWRA model simulations. The top level soil moisture from the GLDAS model shows a rather stable correlation coefficients of about 0.4 in the South, which raises to 0.6-0.7 in the northern part of pass 075 (Fig 7). Top level soil moisture from the AWRA model shows weak correlations (< 0.2) in the south and stronger correlation coefficients (0.5 - 0.6) in the northern part of the pass. The correlations with SMOS products for the time period considered here, show a less reliable behavior with rapidly varying correlation coefficients along the track and become negative in the North.

5.3. Surface Soil Moisture Anomalies within Western Australia

We examine the quality of ARSSM estimations over the entire study regions A and B (Fig. 1). Since the ARSSM results from the C- and Ku-Band of Jason-2 are found to be very similar (compare Fig. 6 and 7), we limit the results to the C-Band covering the period 2008-2014. Generally, C-Band is considered to be more sensitive to surface soil moisture due to the longer wavelength which enables better penetration of the surface. The Ku-Band results are summarized in Table 3 and 4. For Envisat, we limit the discussion to the Ku-Band data (2002-2010) since the time series of the S-Band backscatter data is much shorter due to an instrument failure. Consequently, they are not included in Tables 5 and 6, either.

5.3.1. Soil Moisture within Northwestern Australia (Study Region A)

In Fig. 8 (A) and (B), correlation coefficients between the C-Band backscatter and GLDAS as well as AWRA simulations are shown. The magnitude of the correlation coefficients is found to be small < 0.2 at some locations along the track. Generally smaller correlations are found between altimetry backscatter and AWRA simulations (Fig. 8, (B)) compared to those of GLDAS (Fig. 8, (B)). Similar to the results in Fig. 2, these sudden drops in correlation are mainly detected over regions, where the altimetry footprint contains surface water, e.g., passing over lakes and rivers. This can for example be observed at the crossing point of Jason-2 tracks 151 and 216 (see Fig. 1 (A) approximately at $123.25°E$ and $26.70°S$) over Lake Wells (Fig. 1, (A)), where the return signal includes almost no information related to land surface features.

EOFs are computed from AWRA simulations and used in equation 6 to invert ARSSM. These estimations are then correlated with GLDAS and AWRA model simulations (see Fig. 8 (C) and (D)). Another set of ARSSM is also estimated using GLDAS EOFs, and the correlation with model simulations is shown in Fig. 8 (E) and (F). The ARSSM results indicate higher correlation with model simulations (compare Fig. 8 (A) and (B) to the rest).

Correlation between ARSSM and model simulations is found to be stronger close to the coast in the west and southwest of the study region A. In the central and southern central parts, ARSSM indicates weak to medium correlation with AWRA, and significantly stronger correspondence with GLDAS. In the northwest (along the pass 177 in Fig. 1 (A)) very low correlation coefficients are found in Fig. 8 (C) and (D). We ascribe this to significant topography changes along the altimetry ground track. In the eastern part of region A, along the pass 151 of Jason-2 and from the crossing point with the pass 38 and north of it, a rather large area with very low correlations can be observed. Surface soil moisture simulations from AWRA do not show any variations over the Gibson Desert (Fig 1) during 2008-2011. As a result, low correlations are derived in this region when either EOFs from AWRA are employed (Fig. 8, (C)) or correlations with respect to the AWRA model data are estimated (Fig. 8 (D) and (F)). In contrast, ARSSM based on GLDAS EOFs is close to GLDAS SSM (Fig. 8, (E)) over the Gibson Desert. This effect is well reflected in Table 3 while comparing the minimum correlations with the GLDAS and AWRA model data.

In Fig. 9, correlation between soil moisture products and precipitation (from ERA-Interim) is shown, where the spatial variability of GLDAS (in A) seems to be smoother compared to AWRA (in B). Figure 9 (B) indicates low correlation regions along the Jason-2 pass of 064, 075, and 151 (Fig. 1 (A)) while these do not appear in the GLDAS results (Fig. 9 (A)).

Both ARSSM sets (based on EOFs of GLDAS and AWRA) follow closely precipitation (see Fig. 9 (C) and (D)). The magnitude of the correlations is found to be relatively higher than for of models (compare Fig. 9 (A) and (B) to (C) and (D), see also the values in Table 3).

The variability of soil moisture within the region A is examined by estimating standard deviations at along-track altimetry positions (see also Table 4). Standard deviations between $0.04\,m^3/m^3$ and $0.06\,m^3/m^3$ are found from the GLDAS simulations (Fig. 10 (A)), while the magnitude of AWRA simulations (Fig. 10 (B)) is larger than GLDAS in the southwest. A region of very low standard deviations is found in the eastern part along the tracks 038 and 151 (Fig. 1 (A)) that is located within the Gibson Desert region (Fig. 10 (A)). In the northern and central parts of the study area A, we find medium temporal variations which are slightly larger than those of GLDAS. The overall variability of ARSSM sets depends on the models employed for estimating EOFs used in the inversion (Fig. 10 (A) and (C), and Fig. 10 (B) and (D)). Considering the along-track variabilities, it is clear that ARSSM sets represent higher spatial resolution than models (compare along-track patterns of Fig. 10 (C) with (A), and Fig. 10 (D) with (B)).

In Fig. 11 (A), the magnitude of soil moisture from SMOS is shown which is generally stronger compared to models and ARSSM (in Fig. 10). The SMOS results can independently assess other soil moisture products. For instance, correlation coefficients between ARSSM, employing the EOFs of AWRA, and SMOS are found to be relatively larger (0.6 - 0.8) in many areas. With respect to the eastern part of the study region, along the pass 151 we find low correlations over the Gibson Desert region due to the AWRA base functions used here. Correlations between SMOS and ARSSM based on EOFs from GLDAS in this region agree much better (not shown here). Lower correlation coefficients in the northwestern part are related to the rapid changes in topography within this region (Fig. 11 (B)).

5.3.2. Soil Moisture within Southwestern Australia (Study Region B)

ARSSM estimations (2002-2010), derived from the Ku-Band of Envisat within the study region B (Fig. 1), are examined in this section. The groundtracks of Envisat are denser than those of Jason-2 and they provide the chance to assess the quality of ARSSM over different vegetation classes. In the light of previous results, since selecting EOFs from AWRA or GLDAS does not significantly alter ARSSM estimations, we limit our results to the ARSSM inverted by fitting the EOFs of the AWRA model.

Table 3: An overview over the median, minimum, and maximum correlation between Jason-2 ARSSM and model data from GLDAS, AWRA and ERA-Interim precipitation, as well as SMOS ascending and descending orbits is provided for study area A (Fig. 1, (A)). The individual rows are associated to ARSSM from using Ku- and C-Band, as well as EOFs from either GLDAS or AWRA model data. The number of points used for computation was 29271.

	GLDAS	AWRA	ERA-I	$SMOS_{asc}$	$SMOS_{desc}$
$ARSSM^{Ku}_{GLDAS}$	0.60	0.49	0.55	0.68	0.63
[min max]	[0.19 0.83]	[-0.08 0.81]	[0.19 0.88]	[0.02 0.91]	[-0.23 0.92]
$ARSSM^{C}_{GLDAS}$	0.60	0.48	0.55	0.70	0.65
[min max]	[0.17 0.84]	[-0.16 0.79]	[0.25 0.84]	[-0.05 0.93]	[-0.16 0.92]
$ARSSM^{Ku}_{AWRA}$	0.58	0.48	0.55	0.67	0.61
[min max]	[-0.13 0.83]	[-0.21 0.77]	[-0.20 0.88]	[-0.32 0.90]	[-0.31 0.93]
$ARSSM^{C}_{AWRA}$	0.57	0.46	0.52	0.68	0.63
[min max]	[-0.12 0.85]	[-0.32 0.80]	[-0.23 0.84]	[-0.27 0.93]	[-0.29 0.94]

Table 4: Overview over the median, minimum, and maximum standard deviations (SD) of SSM from ARSSM using Ku- and C-Band, as well as EOFs from AWRA and GLDAS for study area A (Fig. 1, (A)); furthermore, standard deviations from the GLDAS and AWRA model, as well as SMOS ascending and descending orbits are included. Standard deviations are provided in $[m^3/m^3]$. The number of points used for computation was 29271.

	$\mathbf{SD}_{median}$	$\mathbf{SD}_{min}$	$\mathbf{SD}_{max}$
$ARSSM^{Ku}_{GLDAS}$	0.045	0.021	0.068
$ARSSM^{C}_{GLDAS}$	0.046	0.025	0.061
$ARSSM^{Ku}_{AWRA}$	0.059	0	0.096
$ARSSM^{C}_{AWRA}$	0.061	0	0.089
GLDAS	0.044	0.033	0.056
AWRA	0.058	0	0.098
$SMOS_{asc}$	0.061	0.027	0.136
$SMOS_{desc}$	0.051	0.022	0.010

Standard deviations of soil moisture products are shown in Fig. 12 (A), (B), and (C), which indicate stronger variability compared to the region A. Similar signal strength is found between ARSSM and AWRA simulations (∼0.08 and $0.12\,m^3/m^3$ in Fig. 12 (A) and (B)) and relatively larger than that of GLDAS (∼0.04 and $0.06\,m^3/m^3$ in Fig. 12 (C)). This agrees with the results from before (Fig. 10). Considering the ARSSM results in Fig. 12 (A), two small areas with relatively low standard deviations are identified: in the north, where the pass 0950 and 0307 meet (see Fig. 1 (B)) the first area corresponds to the altimeter crossing the Lakes Deborah and Seabrook and the second area in the

Table 5: Overview over the median, minimum, and maximum standard deviations (SD) of SSM from ARSSM using Ku-Band and EOFs from AWRA for study area B (Fig. 1, (B)); furthermore, standard deviations from the GLDAS and AWRA model are included. Standard deviations are provided in $[m^3/m^3]$. The number of points used for computation was 16350.

	$\mathbf{SD}_{median}$	$\mathbf{SD}_{min}$	$\mathbf{SD}_{max}$
$\mathrm{ARSSM}^{Ku}_{GLDAS}$	0.089	0.024	0.163
GLDAS	0.050	0.037	0.070
AWRA	0.089	0.058	0.106

east, along the pass 0778 (see Fig. 1 (B)), is associated with the altimeter crossing Lake Cowan. The return signal from these large surface waters completely dominates the backscatter at these locations, which results in less meaningful ARSSM estimations.

Correlation between ARSSM and AWRA and GLDAS is shown in Fig. 12 (D) and (E), where we find values of more than 0.5 over the central and eastern parts of the region B with land cover classes ranging from dry savanna and shrublands in the eastern parts to large agricultural areas in the center. In the west and southwest, close to the coast, the correlation coefficients are relatively low < 0.2, where the land is covered by dense forest. Additionally, close to Perth located at the west coast (Fig. 1 (B)), we find significantly lower correlations. It is interesting to note that the correlation coefficients of ARSSM with both AWRA and GLDAS are significantly higher in the descending altimetry tracks (even pass numbers in Fig. 1 (B)) than for the ascending tracks (odd pass numbers in Fig. 1 (B)).

ARSSM and 3-day accumulated precipitation data from ERA-Interim (Fig. 12 (F)) are found to be virtually unrelated in the central and western, as well as in the south-eastern parts of the study region. Moderate correlation coefficients are found in the east and northeast parts of the region B. A similar pattern is observed when correlating soil moisture from AWRA simulated model data with 3-day accumulated ERA-Interim precipitation information (not shown here).

Table 6: An overview over the median, minimum, and maximum correlation between Envisat ARSSM and model data from GLDAS, AWRA and ERA-Interim precipitation is provided for study area B (Fig. 1, (B)). The number of points used for computation was 16350.

	GLDAS	AWRA	ERA-I
ARSSM^{Ku}_{AWRA}	0.61	0.55	0.23
[min max]	[-0.09 0.83]	[-0.12 0.89]	[-0.22 0.67]

6. Discussion

6.1. Assessing the Level of Agreement between the ARSSM and Model Simulation/ SMOS

In this study, we first confirmed that there is a good correspondence between altimetry backscatter and available model derived soil moisture simulations within the (semi-)arid region of Western Australia (see Fig. 3). This relationship has already been investigated for other regions (Ridley et al., 1996; Papa et al., 2003; Fatras et al., 2012, 2015). We proceeded to apply altimetry backscatter for estimating surface soil moisture (SSM) information using a novel approach. Before, Fatras et al. (2012) assumed a direct linear relationship between backscatter and SSM. A similar approach was proposed by Wagner et al. (1999) for scatterometer data. In contrast, our approach relies on spatial information based on model data to constrain the altimetry derived backscatter and convert them to the SSM values.

The altimetry backscatter used in this study is a (slightly) modified version of the backscatter from the ICE-1 retracker (Martin et al., 1983), which allows us to suppress the effects of peaks, located on the trailing edge of the waveform, on the backscatter estimations. These peaks are often caused by open water located in the off-nadir direction. After applying the modification in equation (4), smoother backscatter values are derived compared to those from the ICE-1 method (see Fig. 2) especially close to surface waters. Fatras et al. (2012) investigated backscatter from different available retracking methods (while considering Envisat data over Sahel) and concluded that ICE-1 was best suited for deriving SSM. Generally we believe that developing a more specialized retracking method for retrieving land surface backscatter would improve the results.

We interpolated all available data sets spatially and temporally to the altimeter ground track and times of crossing the study areas, respectively. This is an important step since, e.g., simply using model data with a higher temporal resolution to derive the EOFs would introduce artificial features, which may not be resolved by altimetry. The spatial interpolation allows us to handle each altimeter track individually. Fatras et al. (2015) averaged all altimetry data within a defined region in order to compare them with other data with a different spatial resolution. However, we believe that the high along-track resolution of altimetry is one of its greatest benefits and should be kept.

In the next step, the differences between successive cycles are computed to reduce influences from surface features, such as topography, surface roughness and to some extent vegetation, which can be assumed either constant or varying slowly compared to the repeat periods. As a result, we reconstruct anomalies of surface soil moisture rather than absolute values. Other studies (Fatras et al., 2012, 2015) identified significant seasonal cycles in the backscatter values over lands. For Western Australia, we found only a very small annual amplitude in the ARSSM and simulated anomalies. The proposed approach can also be applied to the absolute backscatter observations, without subtracting successive cycles. In this case, one has to remove the seasonal cycles before computing quality measures such as correlation.

Direct comparisons between ARSSM, AWRA model data and SMOS (e.g. Fig. 5) reveal that ARSSM corresponds well to SMOS derived SSM while not necessarily agreeing with the model data although the same models data was used for implementing the inversion. This indicates that our ARSSM is only constrained by the spatial information extracted from the model data but the temporal evolutions carry the characteristics of the backscatter measured by altimetry. The differences between model simulations and ARSSM/SMOS might also be related to the temporal sampling. For example, AWRA produces daily averages of top level soil moisture, which are not identical with altimety samples that are collected in a few minutes from Western Australia.

6.2. Along-Track Behavior of the ARSSM

Along-track correlations between AWRA model data with GLDAS model data, Ku- and C-Band ARSSM, as well as SMOS data (from ascending and descending passes) are investigated (Fig. 6). The results from Ku- and C-Band are closely related although C-Band would theoretically be better suited to derive soil moisture information due to its longer wavelength that allows better penetrating the canopy layers (Fatras et al., 2015). Previous studies have also found little influence from vegetation on the measured nadir backscatter from altimetry (Fatras et al., 2012, 2015), within (semi-)arid regions, which explains the similar performance of the Ku- and C-Band within Western Australia. Higher correlations are found between the ascending SMOS data and ARSSM/model compared to descending orbits. This is likely related to the sampling time i.e $\sim$6h local time at the equator for the ascending and $\sim$18h local time at the equator for the descending orbits (Kerr et al., 2012). For Envisat Ku- and S-Band, Fatras et al. (2012) suggested that computing differences between the two bands likely represent information on soil moisture storage of different depth. However, we find a weak correlation coefficients with AWRA, especially in the South (less than $\sim$0.3 between $24°S$ and $18°S$), and therefore we exclude its discussion in the rest of the study.

Since soil moisture in Australia is primarily driven by precipitation (Bartalis et al., 2007; Draper et al., 2009), we also correlated soil moisture products to 3-day accumulated precipitation anomalies derived from the ERA-Interim reanalysis product (see Fig. 7). The 3-day period is selected following Ridley et al. (1996)'s recommendation that stated in the Australian Simpson Desert the influence from precipitation on measured SSM rapidly starts to fade after about two days. Larger correlation coefficients are found between precipitation and ARSSM compared to model simulations. This indicates that altimetry measurements are more sensitive to wet surface conditions, especially in the first few centimeters of soil. For AWRA, we found weak correlations with precipitation in the South in contrast to relatively higher and stable correlations between GLDAS and precipitation. Weaker correlations of AWRA in the southern part of pass 075 seem to be justified since precipitation is not the sole driver of soil moisture changes in that region. We also find that the surface soil moisture barely increases in the Australian desert regions even after heavy rainfall events, which is related to high evaporation rates in this region (see also Ridley et al., 1996). This is also confirmed by expanding the examination with respect to ARSSM and model data from GLDAS and AWRA to all altimetry tracks in our study region A (Fig. 9).

Correlation coefficients between SMOS products and precipitation are found to be similar to those of ARSSM and precipitation in the south (up tp $25°S$) indicating that SMOS is also sensitive to wet surfaces. In the north, however, unlike all other products, SMOS indicates smaller correlations with precipitation. More research is required to address this inconsistency between SMOS and other soil moisture products.

6.3. Surface Soil Moisture Anomalies within Western Australia

ARSSM based on EOFs from, GLDAS and AWRA model data show better correlation coefficients with GLDAS for all Jason-2 tracks inside study region A (Fig. 1, (A)). This is likely related to the higher temporal resolution of GLDAS, which provides soil moisture values every 3 hours (Rodell et al., 2004). Similarly, higher correlations are found between SMOS and GLDAS compared to SMOS and AWRA.

Strong similarities between Fig. 8 (C) and (E), as well as between Fig. 8 (D) and (F) indicate that introducing EOFs in the inversion acts as a constraint to reduce the noisy behavior of backscatter, and the final ARSSM results do not significantly depend on the chosen model base functions (from AWRA or GLDAS). However, since the spatial resolution of GLDAS is low, one must carefully select the study regions sufficiently large enough to have meaningful EOFs.

Over the Gibson Desert (Fig. 1, (A)), low correlations are found between ARSSM and simulated soil moisture model data (Fig. 8), precipitation (Fig. 9), as well as SMOS observations (Fig. 11, (B)). Low standard deviations are also detected in this region (Fig. 10). Soil moisture simulations from AWRA are not able to reflect the small changes and thus the outputs include only zero values over this region during 2008-2011. As a result, the EOFs derived from AWRA over this region are also zero, which consequently, limits the estimation of ARSSM within this region.

Analyzing the standard deviations indicates that the amplitude of ARSSM (Fig. 10) strongly depends on the standard deviations of a-priori models. For example lower standard deviations are expected from GLDAS since its spatial resolution is lower than AWRA. Comparisons with SMOS (Fig. 11, (A)) indicate closer correspondence with

ARSSM inverted based on the AWRA's EOFs. These findings are also supported by comparing the standard deviations in the study area B (Fig. 1, (B)) for ARSSM based on Envisat backscatter and the two model data sets (Fig. 12, (A)-(C)).

The good correlation between ARSSM and SMOS, as an independent measurement of SSM, indicates that the proposed approach to reconstruct SSM from altimetry works well. Small discrepancies are found over regions in the North, which are co-located with significant elevation anomalies. Rapid elevation changes will affect the retrieved signal on the altimetry satellite since the range window on-board of the satellite is not able to adapt to rapid changes in topography. This effect will be filtered in future implementations of the algorithm.

In the study area B (Fig. 1, (B)), the Envisat Ku-Band data in combination with EOFs derived from AWRA model data are used to derive ARSSM. The results are then correlated with the simulations of AWRA and GLDAS (Fig. 11, (D) and (E)). The ARSSM results are found to be sensitive to the land cover, whereas higher correlations are found over shrublands, savanna and agricultural land compared to dense forests or cities. In such regions, the altimetry signal cannot penetrate well through the trees or buildings and, thus, contains little information about SSM. A similar observation can be made for the correlations with precipitation over agricultural surfaces compared to shrublands or savanna (Fig. 12, (F)). Over agricultural surfaces, the correlation is found to be significantly smaller which is likely related to irrigation during periods of low precipitation.

Higher correlations are found between ARSSM computed from ascending tracks and models compared to the descending tracks. A possible explanation for this effect is the time difference between altimetry measurements. Envisat flies on an almost perfect 35-day repeat orbit. As a result, over region B, all ascending track measurements refer to times between 2pm and 3pm UTC, while all descending measurements are between 1am and 2am UTC. This means that the surface conditions observed by the altimeter are quite different between the night- and day-time, and therefore this difference should be considered for future applications and when comparing to different data sets. Another aspect could be the influence of dew during night-time that has been suggested by Ridley et al. (1996). This effect is reflected in the ARSSM but is not included in the soil moisture model data simulations.

6.4. Residuals of ARSSM and Model Simulations

In Fig. 13, principal component analysis (PCA, equation (5)) is applied to the differences of ARSSM and model simulations, from which only the first dominant mode is shown. To compute the residuals with respect to the AWRA simulations (Fig. 13 (A) and (B)), ARSSM are inverted using the EOFs of AWRA. Similarly, ARSSM in Fig. 13 (C) and (D) are inverted using the EOFs of GLDAS before computing the residuals with GLDAS simulations. Therefore, the residuals are estimated in a consistent manner and indicate the contribution of the new products in improving the estimation of spatio-temporal variability of soil moisture within West Australia. The dominant temporal patterns (Fig. 13 (B) and (D)) do not indicate seasonal differences between ARSSM and model simulations but rather noise-like or related to individual events. The strong peaks in the early 2009 and 2011 coincide with fairly strong precipitation events (precipitation results are not shown). Strong differences with AWRA are found in the northeast of region A, where AWRA is also not consistent with SMOS and GLDAS products. The differences between ARSSM and GLDAS are distributed over the entire region A with stronger anomalies over the southern parts. In the same region, we identify smaller residuals between ARSSM and GLDAS model data. The reason for these differences with GLDAS simulations is mainly related to the coarse resolution of its simulation compared to the sampling of altimetry observations. Residuals between ARSSM and model simulations have also been derived over the region B, but are not discussed here.

7. Conclusion

A novel approach is presented to invert satellite radar altimetry backscatter to surface soil moisture. The conversion is performed via an inversion in which spatial empirical orthogonal functions (EOFs) from model simulations are fitted to backscatter observations, and used to produce altimetry reconstructed surface soil moisture (ARSSM). These new data have high along-track measurement rate, but the separation between individual groundtracks is relatively large leading to a limited spatial coverage.

We have been able to confirm the correspondence between altimetry measured backscatter and land surface features, such as surface roughness, topography, vegetation and, especially, soil moisture. Validations of ARSSM against GLDAS and AWRA simulations indicate higher correlation coefficients compared to directly using the backscatter observations. Along-track investigations also showed ARSSM to compare well to the SMOS L3 products (maximum correlations of more than 0.8). Generally, the ARSSM are found to be in better agreement with the GLDAS model data, independent of the model data employed in the inversion. Stronger correlation coefficients are found between ARSSM and precipitation data compared to those between model simulations and precipitation indicating a higher sensitivity of ARSSM and SMOS to precipitation events. For future work, it makes sense to compare the results to regional high resolution precipitation products, such as those in Jeffrey et al. (2001) or Jones et al. (2009).

In the southern study region, generally, a strong agreement is found between ARSSM and model simulations, where the value of correlation coefficients depends mostly on the land cover below the altimetry track, i.e. showing smaller values over dense forest areas or cities while stronger values are found over shrublands, savanna or agricultural land. Some connections are also found with respect to the time of day, when the altimeter measures backscatter signal. Envisat measurements along the ascending tracks are collected during the night, while all the descending tracks refer to the measurements about 12 hours later during the day. Weaker correlation coefficients are found between the latter and the daily mean soil moisture simulated by the models.

We are confident that backscatter from altimetry can provide an independent additional data set of surface soil moisture to extend and support the information available from existing soil moisture missions, such as SMOS or ASCAT. Starting in 1993, altimeters may be able to provide at least two decades of continuous time series of backscatter measurements along the altimetry tracks. Combining altimetry with spatial information derived from high resolution model data for a specific region allows to measure soil moisture changes with high spatial resolution along the altimetry track. The Surface Water and Ocean Topography (SWOT) mission will allow to not only cover the nadir regions, but also two swaths of about 120km to each side of the ground track, which also shows some potential for measuring soil moisture.

In this study, additional influences on the altimetry backscatter signal by vegetation have not been considered. Although, we expect these influences to be small after computing temporal differences, and due to the nadir looking sensors of the altimeter compared to the side looking radar systems, they might still be significant over strongly vegetated regions, e.g., over the agricultural regions in southwestern Australia. Involving these impacts within the proposed inversion will be considered in the future to further improve the reconstruction. Furthermore, assimilating ARSSM into land surface models should be studied in future research.

Acknowledgments

The authors are grateful to Dr. Luigi Renzullo (CSIRO) and Albert I.J.M van Dijk (ANU) for providing the AWRA simulations and to ESA and AVISO for providing the altimetry data. We are also grateful to NASA and NOAH for providing the GLDAS model simulations. The L3 SMOS data were produced by the Barcelona Expert Centre, a joint initiative of the Spanish Research Council (CSIC) and Technical University of Catalonia (UPC). We would also like to thank 3 anonymous reviewers and the associate editor Tim McVicar for their detailed reviews, which greatly improved the quality of the manuscript.

References

Al-Yaari, A., Wigneron, J., Ducharne, A., Kerr, Y., de Jeu, R., Schalie, R., Rodriguez-Fernandez, N., Drusch, M., Dolman, H., & Mecklenburg, S. (2015). Testing simple regression equations to derive long-term global soil moisture datasets from satellite-based brightness temperature observations. In *2. SMOS Science Conference, Madrid, ESP (2015-05-25 - 2015-05-29)*. URL: `http://prodinra.inra.fr/record/305851`.

Angiuli, E., del Frate, F., & Monerris, A. (2008). Application of neural networks to soil moisture retrievals from l-band radiometric data. In *IGARSS 2008 - 2008 IEEE International Geoscience and Remote Sensing Symposium*. volume 2. doi:`10.1109/IGARSS.2008.4778927`.

AVISO (2015). *OSTM / Jason-2 Products Handbook*. CNES / NASA `http://www.aviso.altimetry.fr`. SALP-MU-M-OP-15815-CN, Issue 1.9.

Bartalis, Z., Wagner, W., Naeimi, V., Hasenauer, S., Scipal, K., Bonekamp, H., Figa, J., & Anderson, C. (2007). Initial soil moisture rretrieval from the metop-a advanced scatterometer (ascat). *Geophysical Research Letters*, *34*. doi:`10.1029/2007GL031088`. L20401.

Birkett, C. M., & Beckley, B. (2010). Investigating the performance of the Jason-2/OSTM radar altimeter over lakes and reservoirs. *Marine Geodesy*, *33*, 204–238.

Blarel, F., Frappart, F., Legrésy, B., Blumstein, D., & Rémy, F. (2015). Altimetry backscattering signatures at Ku and S bands over land ice and ice sheets. In *Proc. SPIE 9637, Remote Sensing for Agriculture, Ecosystems, and Hydrology XVII, 963727 (October 14, 2015)*. doi:`10.1117/12.2194498`.

Brown, G. S. (1977). The average impulse response of a rough surface and its applications. *IEEE Transactions on Antennas and Propagation*, *AP-25*, 67–74.

Chai, S.-S., Walker, J. P., Makarynskyy, O., Kuhn, M., Veenendaal, B., & West, G. (2010). Use of Soil Moisture Variability in Artificial Neural Network Retrieval of Soil Moisture. *Remote Sens.*, *2*, 166–190. doi:`doi:10.3390/rs2010166`.

Chelton, D. B., Ries, J. C., Haines, B. J., Fu, L.-L., & Callahan, P. S. (2001). Satellite altimetry and earth sciences: A handbook of techniques and applications. chapter 1. (pp. 1–132).

Dee, D. P., Uppala, S. M., Simmons, A. J., Berrisford, P., Poli, P., Kobayashi, S., Andrae, U., Balmaseda, M. A., Balsamo, G., Bauer, P., Bechtold, P., Beljaars, A. C. M., van de Berg, L., Bidlot, J., Bormann, N., Delsol, C., Dragani, R., Fuentes, M., Geer, A. J., Haimberger, L., Healy, S. B., Hersbach, H., Hólm, E. V., Isaksen, L., Kållberg, P., Köhler, M., Matricardi, M., McNally, A. P., Monge-Sanz, B. M., Morcrette, J.-J., Park, B.-K., Peubey, C., de Rosnay, P., Tavolato, C., Thépaut, J.-N., & Vitart, F. (2011). The era-interim reanalysis: configuration and performance of the data assimilation system. *Quarterly Journal of the Royal Meteorological Society*, *137*, 553–597. doi:http://dx.doi.org/10.1002/qj.828.

Delwart, S., Bouzinac, C., Wursteisen, P., Berger, M., Drinkwater, M., Martin-Neira, M., & Kerr, Y. H. (2008). Smos validation and the cosmos campaigns. *IEEE Transactions on Geoscience and Remote Sensing*, *46*, 695 – 704.

Deng, X., Featherstone, W. E., Hwang, C., & Berry, P. A. M. (2002). Estimation of contamination of ers-2 and poseidon satellite radar altimetry close to the coasts of australia. *Marine Geodesy*, *Vol. 25*, pp. 259–271. doi:10.108/01490410214990.

Desjonquères, J.-D., Carayon, G., Steunou, N., & Lambin, J. (2010). Poseidon-3 Radar Altimeter: New Modes and In-Flight Performances. *Marine Geodesy*, *33(S1)*, 53–79. doi:10.1080/01490419.2010.488970.

Donohue, R. J., McVicar, T. R., & Roderick, M. L. (2008). Climate-related trends in Australian vegetation cover as inferred from satellite observations, 19812006. *Global Change Biology*, *15*, 1025–1039. URL: http://dx.doi.org/10.1111/j.1365-2486.2008.01746.x. doi:10.1111/j.1365-2486.2008.01746.x.

Draper, C. S., Walker, J. P., Steinle, P. J., de Jeu, R. A. M., & Holmes, T. R. H. (2009). An evaluation of amsre derived soil moisture over australia. *Remote Sensing of Environment*, *113 (4)*, 703–710. doi:doi:10.1016/j.rse.2008.11.011.

Entekhabi, D., Njoku, E. G., O'Neill, P. E., Kellogg, K. H., Crow, W. T., Edelstein, W. N., Entin, J. K., Goodman, S. D., Jackson, T. J., Johnson, J., Kimball, J., Piepmeier, J. R., Koster, R. D., Martin, N., McDonald, K. C., Moghaddam, M., Moran, S., Reichle, R., Shi, J. C., Spencer, M. W., Thurman, S. W., Tsang, L., & Zyl, J. V. (2010). The soil moisture active passive (smap) mission. *Proceedings of the IEEE*, *98*, 704–716. doi:10.1109/JPROC.2010.2043918.

ESA (2007). *Envisat RA2/MWR Product Handbook*. European Space Agency (ESA) https://earth.esa.int/handbooks/ra2-mwr/. URL: https://earth.esa.int/handbooks/ra2-mwr issue 2.2.

ESA (2014). *SMOS Level 2 and Auxiliary Data Products Specifications*. European Space Agency (ESA) https://earth.esa.int/documents/10174/1854583/SMOS_L2_Aux_Data_Product_Specification. URL: https://earth.esa.int/documents/10174/1854583/SMOS_L2_Aux_Data_Product_Specification issue 8/1.

Fatras, C., Frappart, F., Mougin, E., Frison, P.-L., Faye, G., P., B., & Jarlan, L. (2015). Spaceborne altimetry and scatterometry backscattering signatures at C- and Ku-bands over West Africa. *Remote Sensing of Environment*, *159*, 117–133. doi:10.1016/j.rse.2014.12.005.

Fatras, C., Frappart, F., Mougin, E., Grippa, M., & Hiernaux, P. (2012). Estimating surface soil moisture over sahel using envisat radar altimetry. *Remote Sensing of the Environment*, *123*, 496 – 507.

Frappart, F., Fatras, C., Mougin, E., Marieu, V., Diepkilé, A. T., Blarel, F., & P., B. (2015). Radar altimtetry backscattering signatures at Ka, Ku, C and S bands over West Africa. *Physics and Chemistry of the Earth*, *83-84*, 96–110. doi:10.1016/j.pce.2015.05.001.

Glenn, E. P., Doody, T. M., Guerschman, J. P., Huete, A. R., King, E. A., McVicar, T. R., Van Dijk, A. I. J. M., Van Niel, T. G., Yebra, M., & Zhang, Y. (2011). Actual evapotranspiration estimation by ground and remote sensing methods: the australian experience. *Hydrological Processes*, *25*, 4103–4116. URL: http://dx.doi.org/10.1002/hyp.8391. doi:10.1002/hyp.8391.

Jeffrey, S. J., Carter, J. O., Moodie, K. B., & Beswick, A. R. (2001). Using spatial interpolation to construct a comprehensive archive of Australian climate data. *Environ. Model Software*, *16*, 309 – 330. doi:10.1016/S1364-8152(01)00008-1.

Jones, D. A., Wang, W., & Fawcett, R. (2009). High-quality spatial climate data sets for Australia. *Aust. Meteorol. Oceanogr.*, *58*, 233 – 248.

Katul, G. G., Oren, R., Manzoni, S., Higgins, C., & Parlange, M. B. (2012). Evapotranspiration: a process driving mass transport and energy exchange in the soil-plant-atmosphere-climate system. *Reviews of Geophysics*, *50*, RG3002. doi:10.1029/2011RG000366.

Kerr, Y. H., Waldteufel, P., Richaume, P., Wigneron, J. P., Ferrazzoli, P., Mahmoodi, A., Al Bitar, A., Cabot, F., Gruhier, C., Juglea, S. E., Leroux, D., Mialon, A., & Delwart, S. (2012). The smos soil moisture retrieval algorithm. *IEEE Transactions on Geoscience and Remote Sensing*, *50*, 1384–1403. doi:10.1109/TGRS.2012.2184548.

Liou, Y.-A., Liu, S.-F., & Wang, W.-J. (2001). Retrieving soil moisture from simulated brightness temperatures by a neural network. *IEEE Transactions on Geoscience and Remote Sensing*, *39*, 1662–1672. doi:10.1109/36.942544.

Liu, Y. Y., Parinussa, R. M., Dorigo, W. A., De Jeu, R. A. M., Wagner, W., van Dijk, A. I. J. M., McCabe, M. F., & Evans, J. P. (2011). Developing an improved soil moisture dataset by blending passive and active microwave satellite-based retrievals. *Hydrology and Earth System Sciences*, *15 (2)*, 425 – 436. doi:10.5194/hess-15-425-2011.

Martin, T. V., Zwally, H. J., Brenner, A. C., & Bindschadler, R. A. (1983). Analysis and retracking of continental ice sheet radar altimeter waveforms. *J. Geophys. Res.*, *88*, 1608–1616.

Montzka, C., Bogena, H., Weihermüller, L., Jonard, F., Bouzinac, C., Kainulainen, J., Balling, J. E., Loew, A., dall'Amico, J., Rouhe, E., Vanderborght, J., & Vereecken,

H. (2013). Brightness Temperature and Soil Moisture Validation at Different Scales During the SMOS Validation Campaign in the Rur and Erft CCatchment, Germany. *IEEE Transactions on Geoscience and Remote Sensing*, *51*, 1728 – 1743. doi:10.1109/TGRS.2012.2206031.

Mougin, E., Lopes, A., Frison, P.-L., & Proisy, C. (1995). Preliminary analysis of ERS-1 wind scatterometer data over land surfaces. *Int. J. Remote Sens.*, *6*, 391 – 398.

Njoku, E. G., Jackson, T. J., Lakshmi, V., Chan, T. K., & Nghiem, S. V. (2003). Soil moisture retrieval from amsr-e. *IEEE Transactions on Geoscience and Remote Sensing*, *41*, 215 – 229. doi:10.1109/TGRS.2002.808243.

Papa, F., Legresy, B., & Remy, F. (2003). Use of the TopexPoseidon dual-frequency radar altimeter over land surfaces. *Remote Sensing of Environment*, *87*, 136 – 147. doi:10.1016/S0034-4257(03)00136-6.

Piles, M., Camps, A., Vall-llossera, M., Corbella, I., Panciera, R., Rudiger, C., Kerr, Y. H., & Walker, J. (2011). Downscaling SMOS-Derived Soil Moisture Using MODIS Visible/Infrared Data. *IEEE Transactions on Geoscience and Remote Sensing*, *49*, 3156–3166. doi:10.1109/TGRS.2011.2120615.

Preisendorfer, R. (1988). *Principal component analysis in meteorology and oceanography*. Elsevier: Amsterdam.

Ridley, J., Strawbridge, F., Card, R., & Phillips, H. (1996). Radar Backscatter Characteristics of a Desert Surface. *Remote Sensing of Environment*, *57(2)*, 63–78.

Roca, M., Jackson, H., & Celani, C. (2002). RA-2 Sigma-0 Absolute Calibration. In *Proc. of Envisat Validation Workshop, Italy, 9 - 13 December 2002 (ESA SP-531, August 2003)*.

Rodell, M., Houser, P., Jambor, U., Gottschalck, J., Mitchell, K., Meng, C.-J., Arsenault, K., Cosgrove, B., Radakovich, J., Bosilovich, M., Entin, J., Walker, J., Lohmann, D., & Toll, D. (2004). The global land data assimilation system. *Bulletin of the American Meteorological Society*, *85(3)*, 381 – 394.

Rodríguez-Fernández, N. J., Aires, F., Richaume, P., Kerr, Y. H., Prigent, C., Kolassa, J., Cabot, F., Jimnez, C., Mahmoodi, A., & Drusch, M. (2015). Soil Moisture Retrieval Using Neural Networks: Application to SMOS. *IEEE Transactions on Geoscience and Remote Sensing*, *53*, 5991–6007. doi:10.1109/TGRS.2015.2430845.

Rötzer, K., Montzka, C., Bogena, H., Wagner, W., Kerr, Y. H., Kidd, R., & Vereecken, H. (2014). Catchment scale validation of SMOS and ASCAT soil moisture products using hydrological modeling and temporal stability analysis. *Journal of Hydrology*, *519*, 934 – 946. doi:10.1016/j.jhydrol.2014.07.065.

van der Schalie, R., Parinussa, R. M., Renzullo, L. J., van Dijk, A. I. J. M., Su, C.-H., & de Jeu, R. A. M. (2015). SMOS soil moisture retrievals using the land parameter retrieval model: Evaluation over the Murrumbidgee Catchment, southeast Australia. *Remote*, *163*, 70 – 79. doi:10.1016/j.rse.2015.03.006.

Shum, C. K., Ries, J. C., & Tapley, B. D. (1995). The accuracy and applications of satellite altimetry. *Geophysical Journal International*, *121 (2)*, 321–336. doi:10.1111/j.1365-246X.1995.tb05714.x.

SMOS-BEC (2015). *SMOS-BEC Ocean and Land Products Description*. Technical Report Barcelona Expert Centre, Institute of Marine Sciences, CSIC. Barcelona, Spain. Available at: http://cp34-bec.cmima.csic.es/doc/BEC-SMOS-0001-PD.pdf.

Ulaby, F., Moore, R., & Fung, A. (1982). Microwave remote sensing: Active and passive. *Radar Remote Sensing and Surface Scattering and Emission*, *2*.

Vaze, J., Viney, N., Stenson, M., Renzullo, L., van Dijk, A., Dutta, D., Crosbie, R., Lerat, J., Penton, D., Vleeshouwer, J., Peeters, L., Teng, J., Kim, S., Hughes, J., Dawes, W., Zhang, Y., Leighton, B., Perraud, J., Joehnk, K., Yang, A., Wang, B., Frost, A., Elmahdi, A., Smith, A., & Daamen, C. (2013). The Australian water resource assessment modelling system (AWRA). *20th International Congress on Modelling and Simulation, Adelaide, Australia, 1-6 December 2013, www.mssanz.org.au/modsim2013*, .

Wagner, W., Lemoine, G., & Rott, H. (1999). A Method for Estimating Soil Moisture from ERS Scatterometer and Soil Data. *Remote Sensing of Environment*, *70(2)*, 191 – 207. doi:10.1016/S0034-4257(99)00036-X.

Zelli, C. (1999). ENVISAT RA-2 advanced radar altimeter: Instrument design and prelaunch performance assessment review. *Acta Astronaut.*, *44(7)*, 323–333.

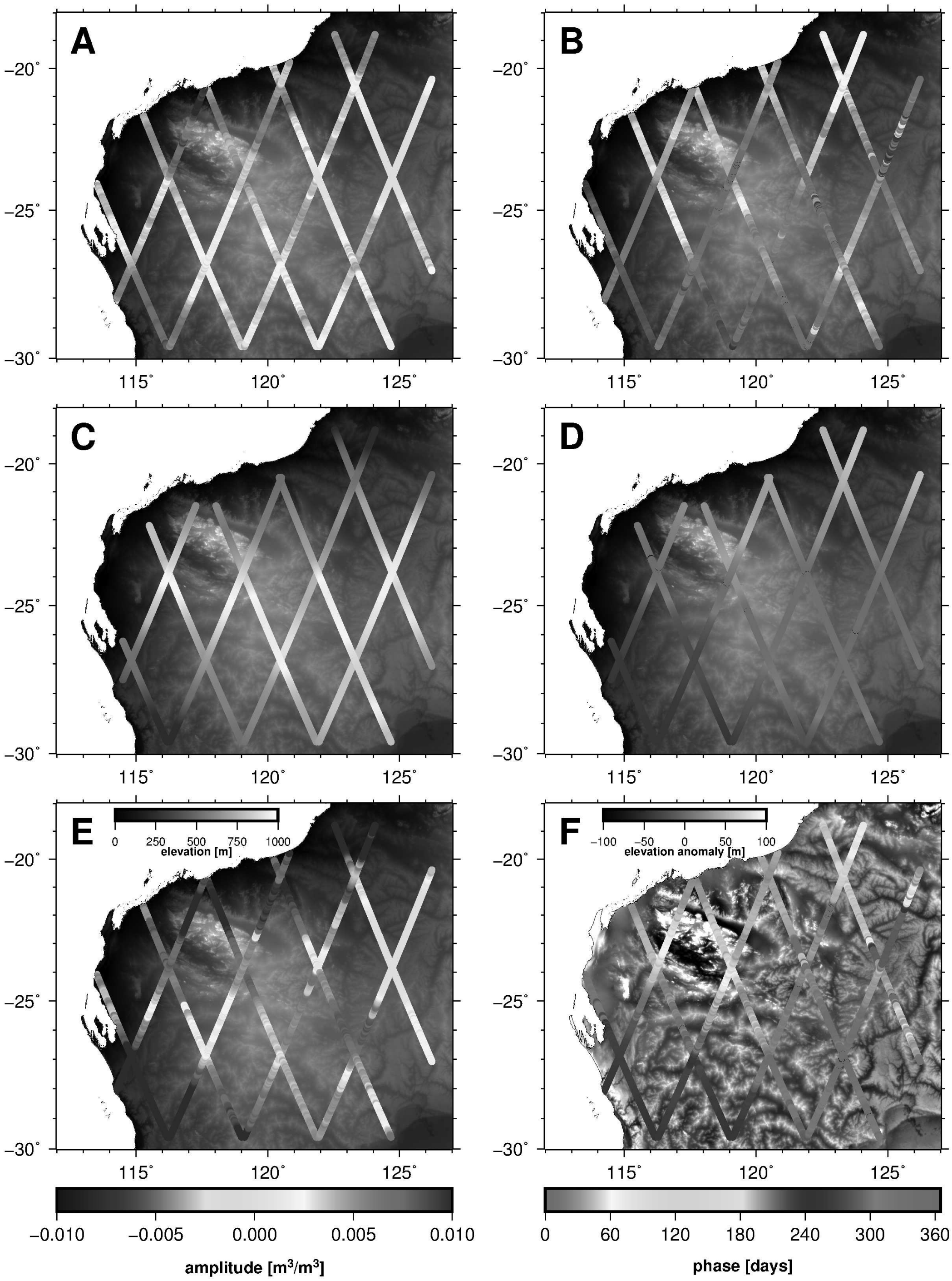

Figure 4: Comparison of annual amplitude and phase from Jason-2 C-Band ARSSM (A) and (B), using spatial base functions derived from the ARWA model, the GLDAS model (C) and (D), as well as the AWRA model (E) and (F).

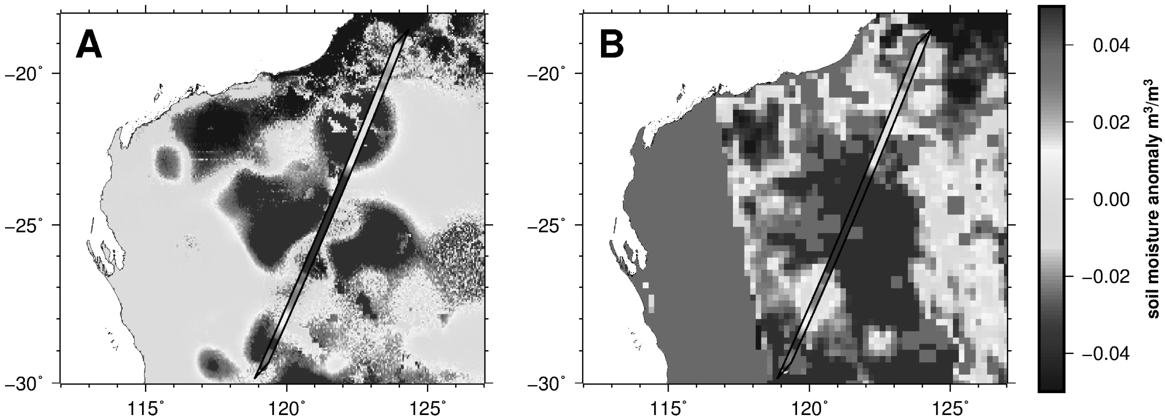

Figure 5: Comparison of soil moisture anomalies from Jason-2, pass 075, cycle 58 (January 31, 2010) with anomalies from (A) AWRA simulation and (B) SMOS products. Colors inside the black polygons represent ARSSM derived from Jason-2 C-Band.

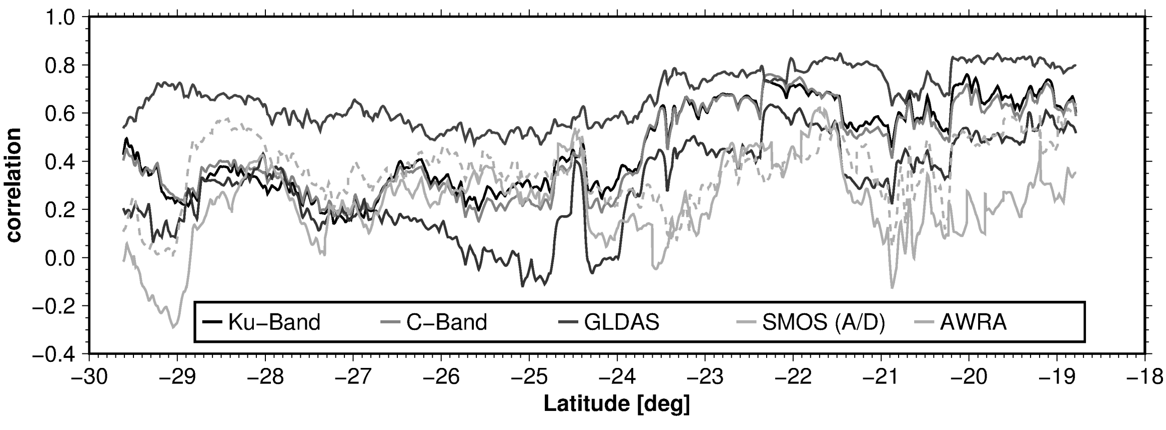

Figure 6: Correlation coefficients between the top level soil moisture anomalies derived from AWRA simulations and those of GLDAS, ARSSM, and SMOS measurements. The results are computed along the pass 075 of Jason-2 for the time period 2008-2011, where AWRA data was available. To estimate ARSSM, the EOFs of AWRA are used in the inversion to convert Ku- and C-Band backscatter measurements to soil moisture anomalies. For SMOS, the solid line refers to the correlation coefficients between descending orbit products and AWRA, while the dashed line corresponds to the ascending orbit products.

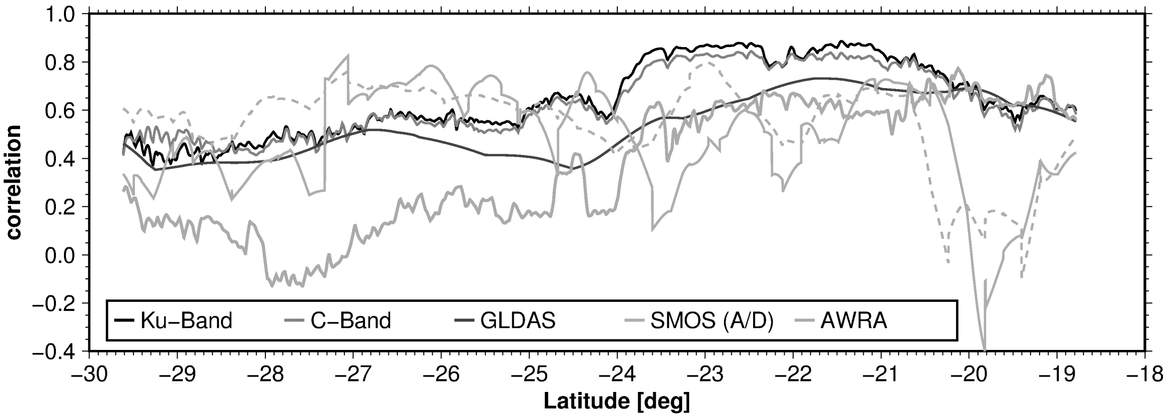

Figure 7: Correlation coefficients (2008-2010) between 3-day accumulated precipitation anomalies from ERA-Interim with ARSSM derived from the Ku- and C-Band of Jason-2 observations, as well as between precipitation anomalies and top level soil moisture information extracted from the GLDAS and AWRA model, and soil moisture derived from SMOS products. For the SMOS data, the solid line refers to the descending orbit, while the dashed line corresponds to the ascending orbit.

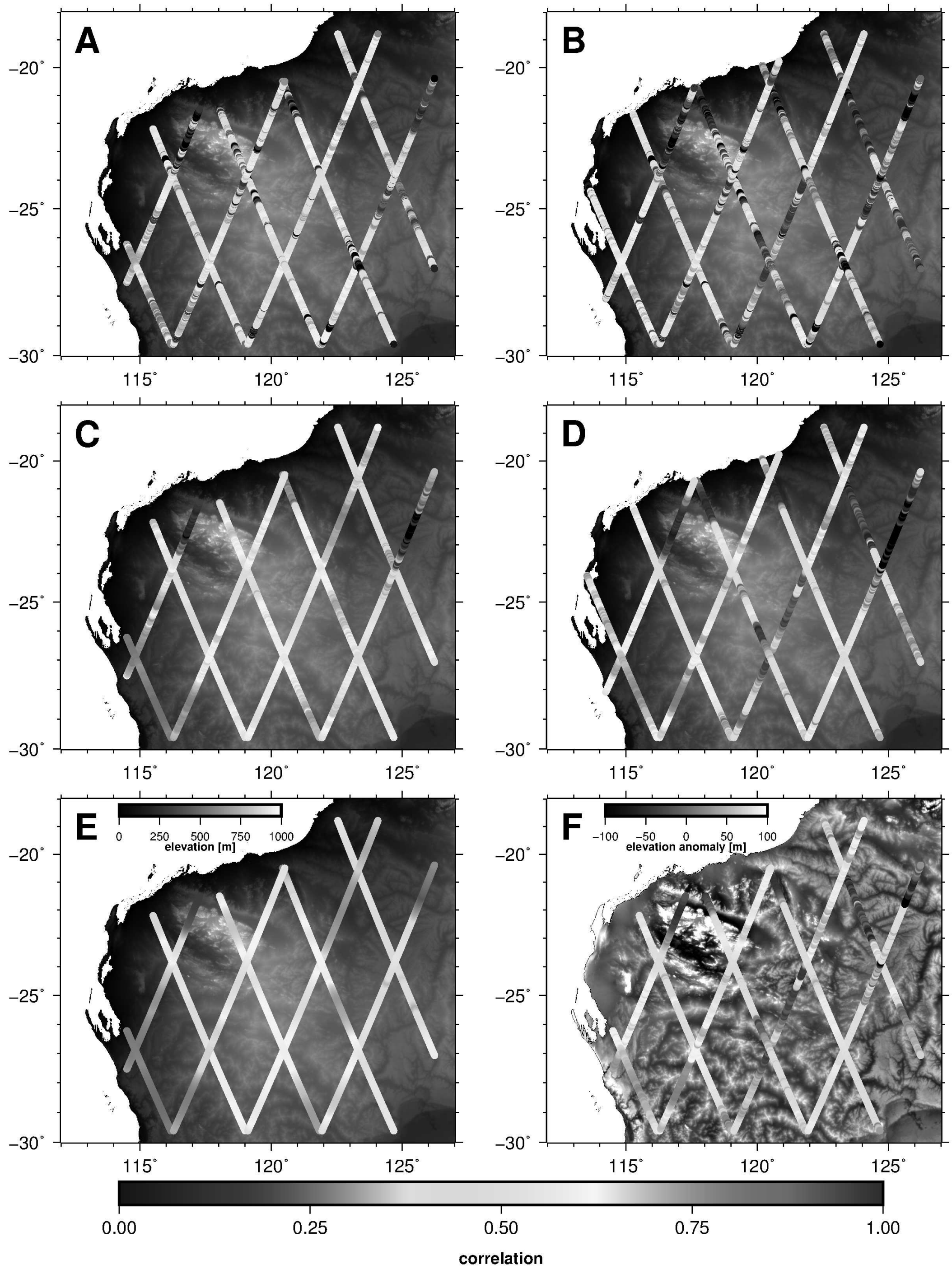

Figure 8: Comparisons between altimetry and model simulations. The first row shows correlations between C-Band backscatter with (A) GLDAS and (B) AWRA model simulations. In the second row, correlations between ARSSM from Jason-2 C-Band using EOFs based on AWRA model data and model data from (C) GLDAS and (D) AWRA are presented. The bottom row, shows correlations between ARSSM derived utilizing GLDAS EOFs and soil moisture model data from (E) GLDAS and (F) AWRA.

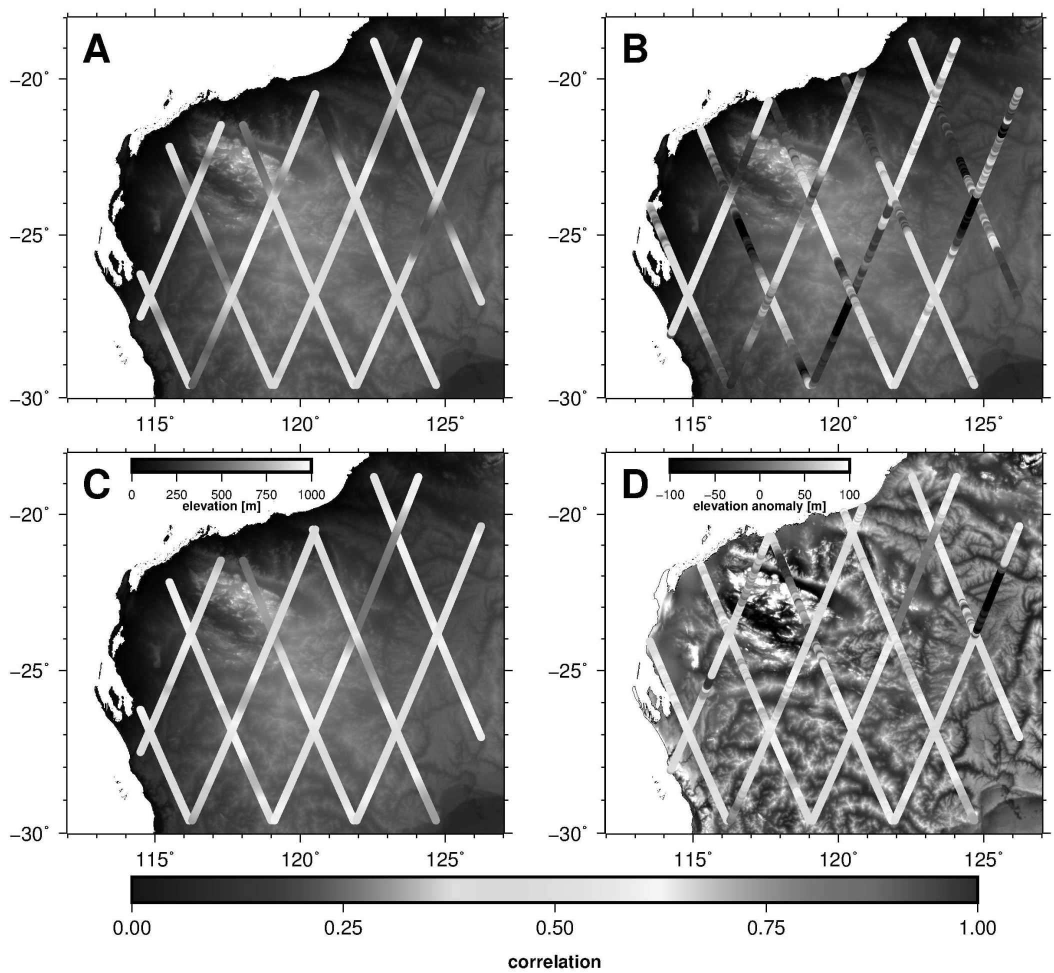

Figure 9: Correlations of ERA-Interim precipitation data with top level soil moisture model data from (A) GLDAS and (B) AWRA. Additionally, correlations between precipitation and ARSSM estimated based on spatial patterns from (C) GLDAS and (D) AWRA are shown.

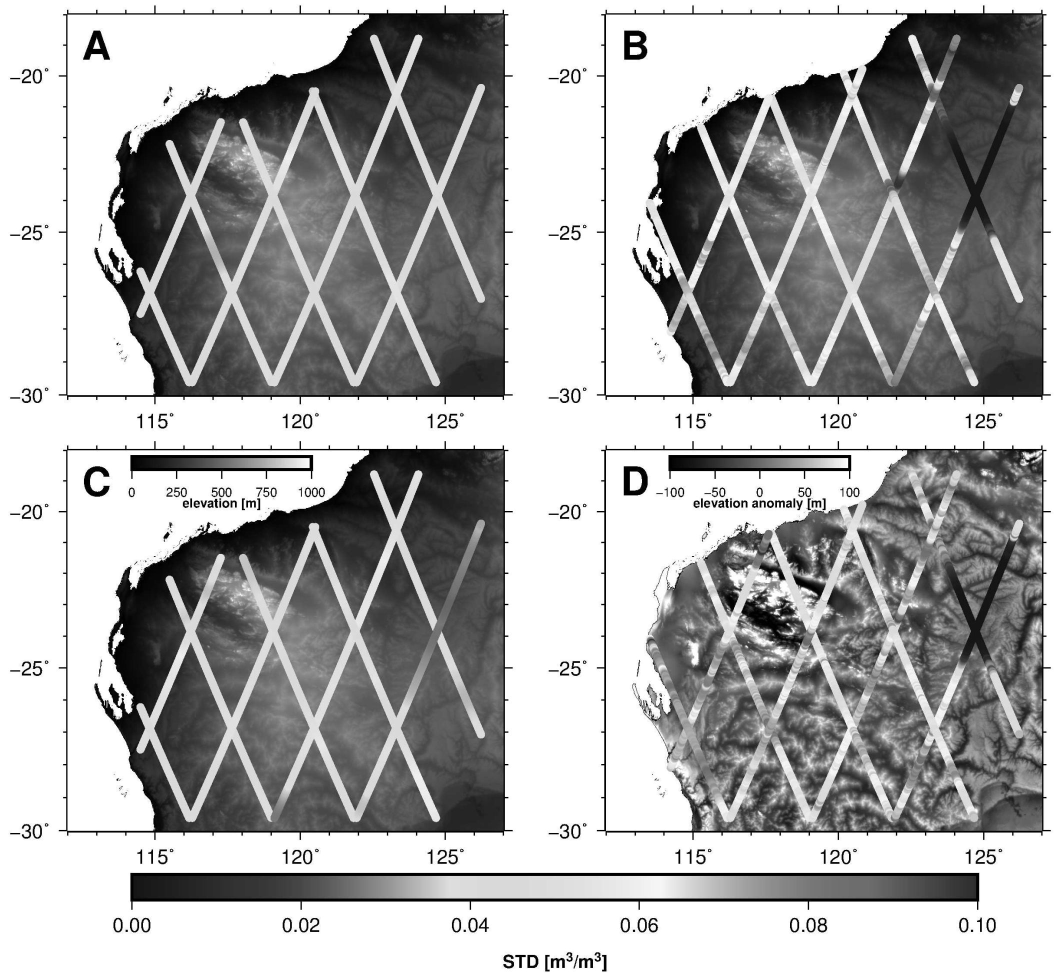

Figure 10: Standard deviations of (A) GLDAS model, (B) AWRA model data, (C) ARSSM based on GLDAS spatial patterns and (D) ARSSM estimated using spatial patterns derived from AWRA.

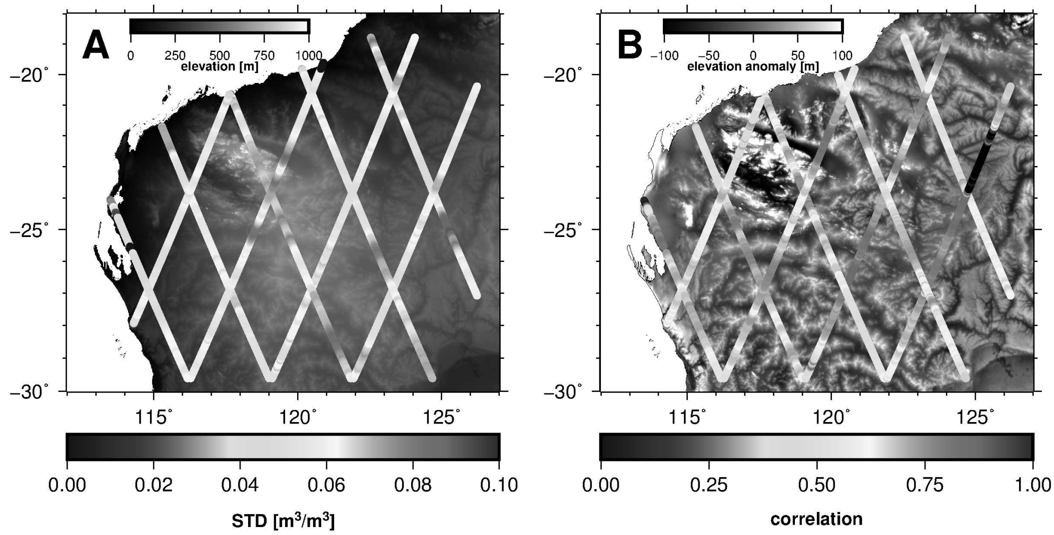

Figure 11: (A) Standard deviations of soil moisture anomalies based on SMOS product. (B) Correlation coefficients between SMOS soil moisture anomalies and ARSSM sets based on the C-Band observations and EOFs of AWRA.

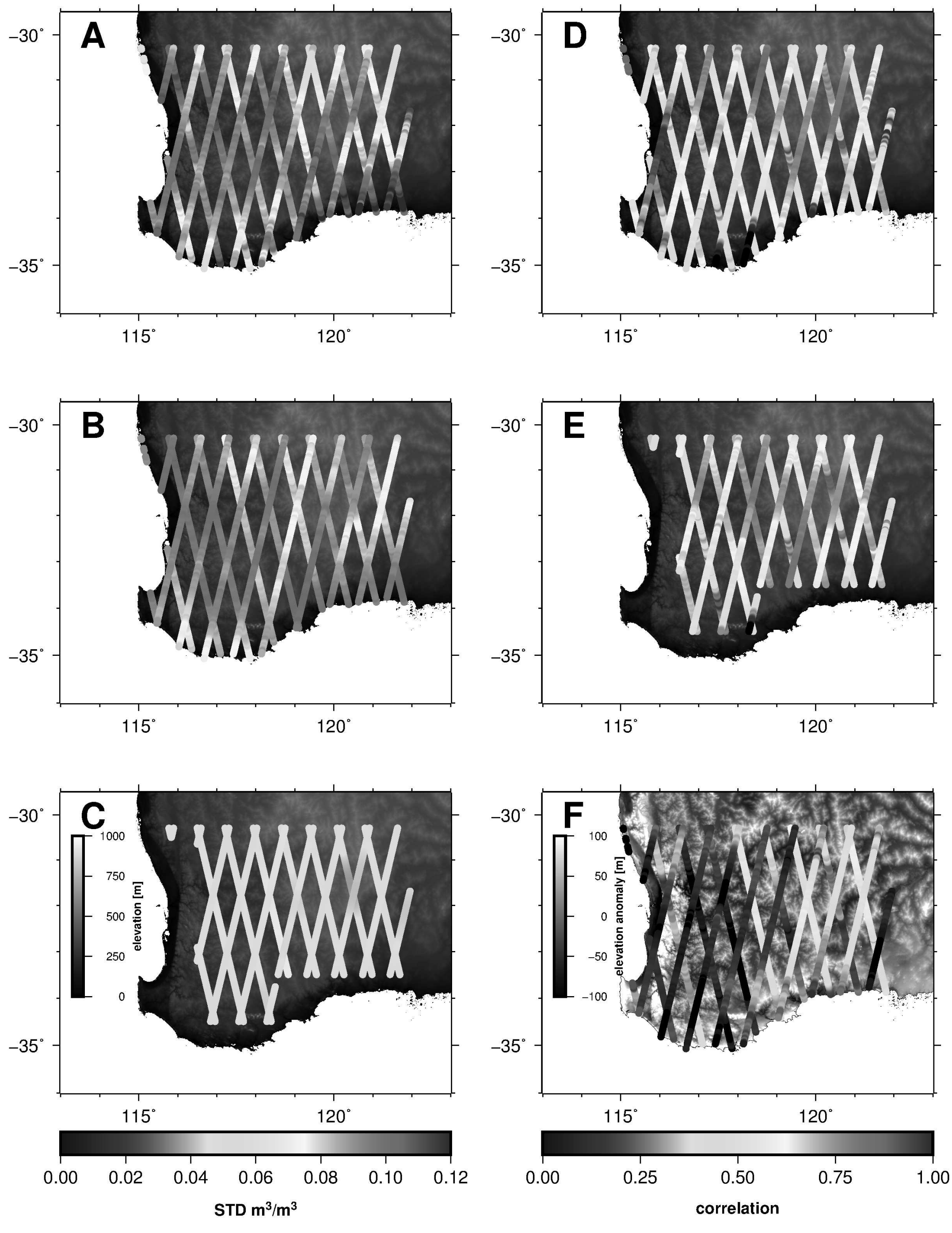

Figure 12: Soil moisture structure during 2002-2010. The first column shows the standard deviations of (A) ARSSM from the Ku-Band of Envisat, (B) AWRA simulations, and (C) GLDAS simulations. The second column includes the correlation coefficients between ARSSM in (A) with (D) AWRA simulations, (E) GLDAS simulations, and finally (E) ERA-Interim precipitation time series.

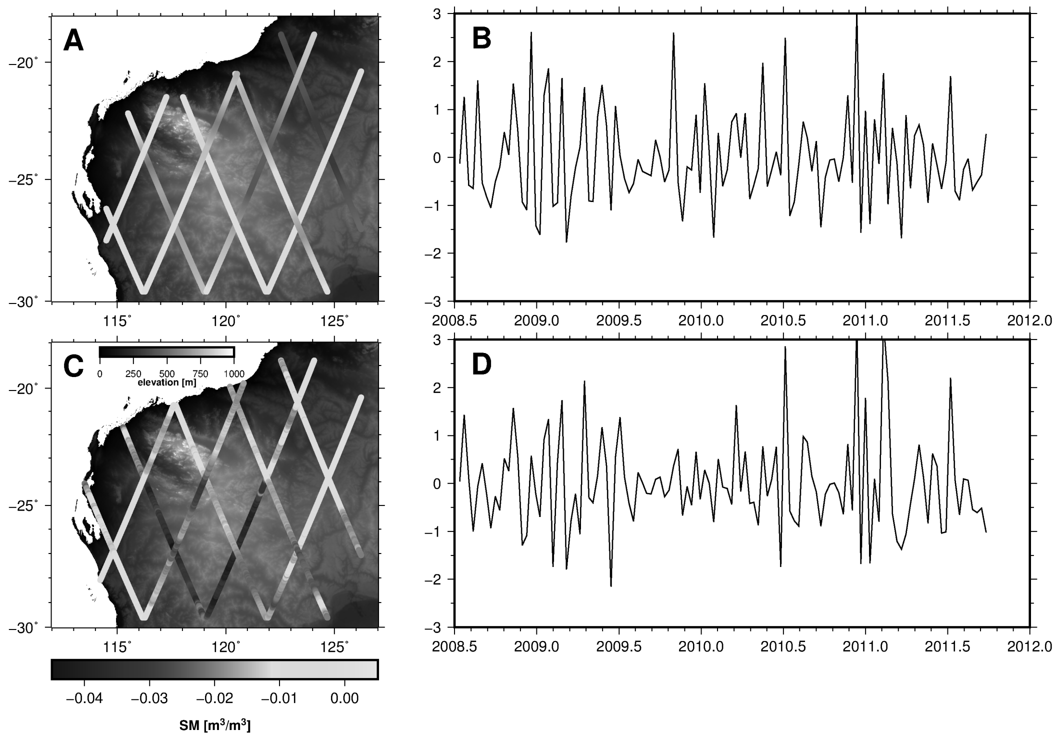

Figure 13: (A) First empirical orthogonal function (EOF) and (B) first principal component (PC) derived by applying SVD on the residuals of ARSSM and GLDAS (explaining 25.0% of the total variance of residuals). (C) First EOF and (D) first PC of the residuals of ARSSM and AWRA (explaining 20.1% of the total variance of residuals).